bioRxiv preprint doi: https://doi.org/10.1101/2020.06.22.166231; this version posted June 23, 2020. The copyright holder for this preprint (which was not certified by peer review) is the author/funder. All rights reserved. No reuse allowed without permission.

The Biomechanical Basis of Biased Epithelial Tube Elongation

Steve Runser[1,2,#], Lisa Conrad[1,2,#], Harold Gómez[1,2,#], Christine Lang[1,2,#], Mathilde Dumond[1,2], Aleksandra Sapala[1,2], Laura Kramps[1,2], Odysse Michos[1,2], Roman Vetter[1,2,*], Dagmar Iber[1,2,*].

Affiliations:

[1] Department of Biosystems, Science and Engineering (D-BSSE), ETH Zurich, Mattenstraße 26, 4058 Basel, Switzerland

[2] Swiss Institute of Bioinformatics (SIB), Mattenstraße 26, 4058 Basel, Switzerland

[#] These authors contributed equally.

* Corresponding authors: Roman Vetter roman.vetter@bsse.ethz.ch and Dagmar Iber dagmar.iber@bsse.ethz.ch

Keywords: Epithelial Tube, Directional Growth, Light-sheet Imaging, Computational Model, Shear Stress, Cell-based Tissue Simulations

bioRxiv preprint doi: https://doi.org/10.1101/2020.06.22.166231; this version posted June 23, 2020. The copyright holder for this preprint (which was not certified by peer review) is the author/funder. All rights reserved. No reuse allowed without permission.

ABSTRACT

During lung development, epithelial branches expand preferentially in longitudinal direction. This bias in outgrowth has been linked to a bias in cell shape and in the cell division plane. How such bias arises is unknown. Here, we show that biased epithelial outgrowth occurs independent of the surrounding mesenchyme. Biased outgrowth is also not the consequence of a growth factor gradient, as biased outgrowth is obtained with uniform growth factor cultures, and in the presence of the FGFR inhibitor SU5402. Furthermore, we note that epithelial tubes are largely closed during early lung and kidney development. By simulating the reported fluid flow inside segmented narrow epithelial tubes, we show that the shear stress levels on the apical surface are sufficient to explain the reported bias in cell shape and outgrowth. We use a cell-based vertex model to confirm that apical shear forces, unlike constricting forces, can give rise to both the observed bias in cell shapes and tube elongation. We conclude that shear stress may be a more general driver of biased tube elongation beyond its established role in angiogenesis.

bioRxiv preprint doi: https://doi.org/10.1101/2020.06.22.166231; this version posted June 23, 2020. The copyright holder for this preprint (which was not certified by peer review) is the author/funder. All rights reserved. No reuse allowed without permission.

INTRODUCTION

Epithelial tubes are an essential component of many organs. During development, epithelial tubes elongate (Fig. 1A). Tube elongation can be either isotropic or anisotropic, i.e. the tubes either lengthen as much as they widen, or there is a bias in outgrowth (Fig. 1B). Growth is by default isotropic, and a bias in elongation can therefore only arise if growth symmetry is broken in the epithelium. How this symmetry break is achieved is largely elusive. We will focus here on the mouse embryonic lung and kidney. In the mouse lung, epithelial tube expansion is anisotropic initially (E10.5-E11.5), but, at least in the trachea, becomes isotropic at later stages (from E12.5) (Kishimoto et al., 2018; Tang et al., 2011; Tang et al., 2018). The biased outgrowth has been related to a bias in the orientation of the mitotic spindles of dividing cells (Saburi et al., 2008; Tang et al., 2011; Tang et al., 2018; Yates et al., 2010). According to Hertwig's rule (Hertwig, 1884), cells divide through their mass point and perpendicular to their longest axis. Indeed, the bias in cell division is accompanied by a bias in cell shape (Tang et al., 2011; Tang et al., 2018). The planar cell polarity (PCP) pathway plays an important role in regulating the mitotic spindle angle distribution in many organs, including the embryonic renal tubes (Ciruna et al., 2006; Gong et al., 2004; Saburi et al., 2008), though no such involvement could be ascertained for the early stages of lung development (Tang et al., 2011). Independent of whether the PCP pathway is involved, it remains an open question how the elongation bias and its direction arise in the first place.

In principle, a bias in outgrowth could originate from polarization along the tube, from a pulling force at the tip, or from a mechanical constraint that limits expansion in the circumferential direction. Several signalling pathways are known to affect the bias in lung tube elongation. Thus, hyperactive KRas ($KRas^{G12D}$) in the lung epithelium abrogates the bias in outgrowth during lung branching morphogenesis (Tang et al., 2011), and pharmacological reagents that activate or inhibit fibroblastic growth factor (FGF) signalling, sonic hedgehog (SHH) signalling, or L-type Ca2+ channels affect the width of cultured lung buds (Goodwin et al., 2019). FGF10 and Glial cell line-derived neurotrophic factor (GDNF) signalling are necessary for the formation of branches in the lung and kidney, respectively (Michos et al., 2010; Min et al., 1998; Moore et al., 1996; Pichel et al., 1996; Rozen et al., 2009; Sanchez et al., 1996; Sekine et al., 1999). FGF10 has been proposed to act as chemoattractant because it is secreted from the submesothelial mesenchyme, and isolated lung epithelia grow towards an FGF10 source (Park et al., 1998). However, *Gdnf* is expressed uniformly in the ureteric cap mesenchyme (Hellmich et al., 1996), and branching morphogenesis is still observed when *Fgf10* is expressed uniformly in the lung mesenchyme (Volckaert et al., 2013), which contradicts a need for a chemoattractant gradient. In both cases, a Turing mechanism may lead to the emergence of focused FGF10-FGFR2b and GDNF-RET signalling at the branch points, despite the uniform expression of the ligand (Menshykau et al., 2014; Menshykau et al., 2019). Focused signalling could then, in principle, result in epithelial leader cells as have been identified in the *Drosophila* trachea and the mammalian kidney (Chi et al., 2009; Ghabrial and Krasnow, 2006). Also, the mesenchymal tip could, in principle, drive elongation as observed in the chick Wolffian duct, where FGF8 prevents a transition to an epithelial state and drives tissue elongation by promoting migratory and motile properties in the mesenchymal tip cells (Atsuta and Takahashi, 2015).

Alternatively, mechanical constraints may drive tube elongation, as proposed for the mammary gland (Paine et al., 2016). Lungs and kidneys do not have a myoepithelium like mammary glands, but smooth muscles could, in principle, drive tube elongation either by providing a mechanical barrier or by promoting peristaltic fluid movement inside the tubes (Jesudason et al., 2006). However, in kidneys, smooth muscles develop only next to the ureter and are not required for tube elongation (Bush et al., 2006). Similarly, in the mouse, biased outgrowth is already noted before airway smooth muscles (ASM) are first observed at E11.5 (Hines et al., 2013; Tang et al., 2011); peristaltic contractions are observed only from E12.5 (Schittny et al., 2000). Moreover, inactivation of *Myocardin* prevents ASM differentiation, but does not prevent lung branching morphogenesis, and results in thinner, rather than wider branches (Young et al., 2020). Therefore, smooth muscles can be ruled out as a necessary driver of biased lung tube elongation. Importantly, branch shape is normal when *Mylk*, which encodes myosin light chain kinase (MLCK), an essential factor for ASM contraction, is inactivated during lung development (Young et al., 2020). This suggests that ASM cells may affect tube diameter via non-mechanical cues.

bioRxiv preprint doi: https://doi.org/10.1101/2020.06.22.166231; this version posted June 23, 2020. The copyright holder for this preprint (which was not certified by peer review) is the author/funder. All rights reserved. No reuse allowed without permission.

In this paper, we sought to systematically analyse the minimal requirements for biased epithelial tube elongation. To this end, we cultured mouse embryonic lungs and kidneys under different conditions and quantified the length and width of the branches for up to 60h. We show that the mesenchyme is not necessary as biased elongating outgrowth is still observed when epithelial buds are cultured on their own, in the absence of mesenchyme, with uniformly dispersed growth factors. Furthermore, we show that while ERK signalling concentrates at the tip of branching isolated epithelial tubes, there is no evidence for the formation of actin-rich protrusions at the epithelial tips that could guide the biased elongating outgrowth. In early lung and kidney development, epithelial tubes only have a narrow luminal space, and tubular cross-sections are often elliptical rather than round. Despite the non-uniform curvature of such closed tubes, tension, as monitored with actin staining, remains uniform in the epithelium. We show that the predicted shear stress level in the narrow embryonic tubes is within the range that cells can, in principle, sense, and a cell-based model confirms that a tangential apical force, as provided by shear stress, can result in the reported bias in cell shape and elongating outgrowth.

RESULTS

Biased epithelial lung tube elongation

Given the reports that the trachea switches from anisotropic to isotropic expansion around E12.5 (Kishimoto et al., 2018), we sought to measure the length and circumference of the bronchus of the left lobe (LL) between E10.5 and E14.5. For this, we used the $Shh^{GC/+}$; $ROSA^{mT/mG}$ transgenic mouse line, which expresses green fluorescent protein (GFP) in the cell membrane of the lung epithelium (Fig. 1A, C, D). Here, we averaged the circumference over the entire 3D bronchus, except for the parts where side branches form (Fig. S1). We confirm the previously reported 2-fold stronger longitudinal than circumferential expansion between E10.5 and E11.5 (Tang et al., 2011), and find that, much as in the trachea, there is a switch to isotropic growth at later stages, though a day later (E13.5) than in the trachea. The substantial widening of the bronchus thus occurs after the emergence of cartilage and smooth muscles (Hines et al., 2013; Schittny et al., 2000). Between E11.5 and E13.5, the bronchus still lengthens more than it widens, even though the overall rate of growth declines (Fig. 1E).

Each 3D length measurement in Fig. 1D,E comes from a different embryo, and we notice a certain level of variability between the specimen. Part of the differences can be accounted to differences in developmental progress, that is observed even in embryos from the same litter. To establish a reliable time line of the growth process, we cultured E11.5 embryonic lungs for 48h on a filter and measured the lengths and average diameter of the branches (Fig. 1F, Fig. S1). Given the development on a filter, there are differences in the branch angles, and much as for the 3D specimens, there is considerable variability between lungs. Nonetheless, in all specimens, we observe a similar biased expansion of the left bronchus (Fig. 1D,E, grey) as in the serially isolated embryonic lungs (Fig. 1D,E, green). The cultured lungs elongate slightly less than in the embryo, and there is less of a reduction in the branch width, though this difference may reflect differences in the analysis. The width in the 2D cultures was averaged along the entire branch (Fig. 1F), while the averaged circumference of the 3D specimen excluded the parts where branches emerge (Fig. S1). Overall, the cultured lungs recapitulate the growth process in the embryo very well, and we will therefore use these to analyse the mechanisms that drives elongating outgrowth.

Mesenchyme is not required for biased epithelial tube elongation during lung and kidney development

While smooth muscles have recently been shown to be dispensable for lung branching morphogenesis (Young et al., 2020), the mesenchyme is well known to affect branch shapes (Blanc et al., 2012; Lin et al., 2003; Sakakura et al., 1976). We, therefore, sought to analyse the impact of the mesenchyme on biased epithelial outgrowth. To this end, we cultured both control lungs and kidneys (Fig. 2A, C, Video S1, S2) as well as explants, where the epithelium was enzymatically separated from the mesenchyme (Fig. 2E, G, Video S3, S4). We used homogeneously distributed suitable growth factors in each case (Materials and

bioRxiv preprint doi: https://doi.org/10.1101/2020.06.22.166231; this version posted June 23, 2020. The copyright holder for this preprint (which was not certified by peer review) is the author/funder. All rights reserved. No reuse allowed without permission.

Methods), and analysed the three lateral domain branches in the left bronchus (LL1-LL3), and two branches in the ureteric bud (UB). We find that these five branches all decrease in their average diameter as they elongate (Fig. 2A-D). As a result, the elongation bias is even more pronounced than for the left lung bronchus. Both lung and ureteric buds still show biased elongating outgrowth when cultured in the absence of mesenchyme (Fig. 2F-H). This excludes a possible wall-like restrictive force, a pulling force, or other polarity cues from the mesenchyme as a necessary driver of epithelial tube elongation. It also confirms that smooth muscles are not necessary for biased elongating outgrowth. We note, however, that in the case of the ureteric bud, the branches elongate less and remain wider in the absence of mesenchyme. This shows that the mesenchyme impacts the elongation process, even though it is not necessary for biased elongation.

Biased outgrowth is not the result of FGF signalling at the tip

Given that biased epithelial outgrowth occurs while isolated explants are exposed to uniform growth factor concentrations (Fig. 2), a necessary polarity in the form of an external growth factor or morphogen gradient can be ruled out. However, as branching is still observed with homogeneous distributions of FGF10 and GDNF (Fig. 2), FGF10 and GDNF signalling must still concentrate at branch points (Fig. 3A); presumably because of a Turing mechanism (Menshykau et al., 2014; Menshykau et al., 2019). ERK signalling is indeed observed to localize at the tips in the embryonic lungs (Fig. 3B), kidneys (Fig. 3C), as well as in mesenchyme-free cultures (Fig. 3D). Accordingly, signalling differs at the tips, and a pulling force from the tip could, in principle, drive the uniform biased outgrowth along the entire tube (Fig. 3E). However, no actin-rich protrusions, such as filopodia or lamellipodia, are observed at the basal epithelial tips, and actin is instead enriched along the apical luminal surfaces (Fig. 3F, G, arrows). Finally, while the FGF receptor (FGFR) inhibitor SU5402 reduces the overall growth rate, it does not reduce the elongation bias (Fig. 3H, Fig. S2, Video S5). This is inconsistent with a role for focused epithelial FGF signalling as a driver of biased elongating outgrowth.

Mechanically forced tube collapse does not result in directional cues for uniform biased outgrowth

Cross-sections of a mouse embryonic lung reveal elliptical tissue shapes with closely opposing apical sides and narrow luminal spaces (Fig. 4A, yellow outlines). Wider lumina are only observed close to branch points and in the tips (Fig. 4A, blue outlines). Collapsed tubular morphologies are not the result of either tissue processing or clearing, as they are also observed in developing lungs cultured in a light-sheet microscope for over 34h (Fig. 4B, Fig. S3, Video S6). Similar observations are made in embryonic kidneys (Fig. 4C).

To explore the possible mechanical effects that can lead to the observed collapse of epithelial tubes, and whether this could provide cues for biased tube outgrowth, we conducted continuum-mechanical finite element simulations in a two-dimensional cross-section perpendicular to the tube axis (Fig. 5A). In our numerical model, the tubular epithelial tissue was represented by an isotropic, linearly viscoelastic continuum, neglecting the cellular structure of the tissue. The epithelial material properties were therefore characterized by a Young modulus E and a Poisson ratio ν. As an initial condition, we chose a tubular shape with uniform radius R (measured from the cylinder axis to the middle of the tissue), and the relative tissue thickness was set to t/R=0.5. The epithelium was set to be intrinsically uncurved, such that a stress-free configuration would be a flat tissue. We used a custom-built finite element simulation framework (Vetter et al., 2013) (Materials and Methods).

We considered three different collapse scenarios. In the first, a uniform net pressure difference ΔP was applied, corresponding to either a pressure drop in the lumen or an increased pressure exerted onto the epithelium by the external environment. The pressure was increased until the critical point of collapse was surpassed. In the second scenario, the epithelial tube was pinched by two rigid parallel clamps slowly approaching one another, mimicking external spatial constraints imposed by a stiff surrounding medium. In the third scenario, the enclosed lumen volume V was controlled with a Lagrange multiplier and

bioRxiv preprint doi: https://doi.org/10.1101/2020.06.22.166231; this version posted June 23, 2020. The copyright holder for this preprint (which was not certified by peer review) is the author/funder. All rights reserved. No reuse allowed without permission.

drained over time until the tube was sufficiently collapsed. Figure 5B shows the equilibrated simulation results for each of the three scenarios. In all cases, both the hoop stress and curvature profiles along the tissue midline are highly nonuniform. Hoop stress is localized almost exclusively in the two extremal points with large curvature. We conclude that, given their non-uniform distribution in the tube cross-section, the stress and curvature patterns that arise from the deformation cannot serve as cues for uniform biased outgrowth.

Stresses can be relaxed rapidly in tissues. We tested experimentally whether the most curved parts remain under increased tension. We find that antibody staining for actin, a read-out for tension in a tissue, is uniform in the closed lung tubes, indicating that there is no increased tension in the curved parts (Fig. 5C,D). It remains possible that a wall-like constraint, in combination with rapid stress relaxation, enforces the elliptic shape and elongating outgrowth. However, it is unclear how such an outer wall-like constricting force would arise even in the absence of mesenchyme. Moreover, we have shown before that a constricting force that results in the observed biased epithelial outgrowth in a cell-based model is insufficient to generate the observed bias in cell shape and cell division (Stopka et al., 2019). Consequently, the mechanical constraints explored here are unlikely to drive the biased elongating outgrowth of embryonic lung tubes.

Shear stress in the developing lung

The developing lung epithelium secretes fluid into the luminal space (George et al., 2015; Nelson et al., 2017). Fluid flow results in shear stress, i.e., in forces that act tangentially on the apical side of the epithelial cells (Fig. 6A). To evaluate the shear stress levels on the apical side of embryonic lungs, we simulated Stokes flow through the lung tube of an E11.5 embryo (Fig. 5B). The lung tube geometry was obtained by segmenting a 400 μm section between the carina and the first branch of the left lung lobe of an E11.5 lung (Fig. 6B, top inset). The average luminal width is about 2 μm (Fig. 6B, bottom inset). We note that given the strong fluorescence on the apical side, the segmentation was possible only in subapical layer. Accordingly, the extracted geometry had a luminal minor axis of 20 μm, which we computationally reduced to the measured luminal minor axis of 2 μm . The viscosity of the fluid in the lung lumen has been measured to be 10 times higher than that of water, i.e. $\mu = 0.016\, Pa \cdot s$ (Bokka et al., 2015), and the flow rate has been estimated as $\dot{V} = 420\ \mu m^3/s$ (George et al., 2015). With these values, we find that the shear stress is highest on the flat part of the embryonic lung tube, and mostly in the range 0.5-1 Pa (Fig. 6B). As we computationally alter the luminal width, we find that the average level of shear stress on the apical surface can be well approximated from a Hagen-Poiseuille flow profile in an elliptical tube of equivalent size (Fig. 6A, C). With the original extracted shape (20 μm along its minor axis), the predicted shear stress level is therefore about 10^{-3} Pa.

Cells sense shear stress with their cilium (Weinbaum et al., 2011). Epithelial kidney cells are particularly sensitive, with renal collecting duct chief cells responding to apical shear stress as low as $6.8 \cdot 10^{-4}$ Pa (Resnick and Hopfer, 2007), and cultured epithelial kidney epithelial cells responding to 0.075 Pa, but not to 1.5 Pa (Nauli et al., 2003). On the other end of the spectrum, endothelial cells are particularly insensitive and typically respond to 0.5-5 Pa (Weinbaum et al., 2011). Cornelial epithelial cells respond to 0.4-0.8 Pa (Molladavoodi et al., 2017), while alveolar epithelial cells respond to 0.7-1.5 Pa (Flitney et al., 2009). The sensitivity of epithelial cells in mouse embryonic lungs and kidneys has not yet been reported, but is likely in a similar range. Accordingly, cells should be able to sense apical shear stress with the measured luminal width. Consistent with a role of shear stress in driving elongating outgrowth, in embryonic lungs that express the constitutively active form $KRas^{G12D}$ in the epithelium ($Shh^{cre/+}$;$KRas^{LSL-G12D/+}$), which disrupts the primary cilium (Tape et al., 2016), the bias in cell division and epithelial outgrowth is lost (Tang et al., 2011).

The pressure gradient in the lumen could also, in principle, impact on tube width directly through a fluid-structure interaction (FSI). To obtain a flow from the bud tips to the opening of the trachea, the fluid pressure must be highest at the tip and smallest at the tracheal opening (Fig. 6D). In case of a FSI, the shape of the branches would then depend on the local fluid pressure, and buds should be wider than stalks. While stalks are indeed thinner than buds, there is no direct dependency of branch width on the

bioRxiv preprint doi: https://doi.org/10.1101/2020.06.22.166231; this version posted June 23, 2020. The copyright holder for this preprint (which was not certified by peer review) is the author/funder. All rights reserved. No reuse allowed without permission.

distance from the tracheal opening (Fig. 6E, Fig. S4, Video S7). A simple way to modulate the pressure at the tips is by altering the distance between the tips and the outlet by culturing lungs either with or without their trachea (Fig. 6E). Removal of the trachea shortens the distance to the outlet, and thus, in case of a constant pressure gradient and flow rate, reduces the pressure difference between the tips and the outlet. We find, however, that a removal of the trachea neither impacts branching morphogenesis nor tip shapes (Fig. 6E,F), which rules out a significant mechanical impact of the fluid pressure on the surrounding epithelium.

Shear stress forces can result in the observed bias in cell shape and outgrowth

In a final step, we investigated whether shear stress, which results in a biased force in the longitudinal direction (Fig. 6A), could recapitulate the observed bias in the apical cell shapes, cell division, and elongating outgrowth (Fig. 7A). We implemented a 2D vertex model (Fig. 7B) using the open-source software Chaste (Fletcher et al., 2013; Mirams et al., 2013). The model has eight biophysical parameters (Supplementary Table 1). With the standard parameters (Fletcher et al., 2013), we can reproduce the characteristics of epithelial polygonal lattices (Fig. S6) (Kokic et al., 2019; Vetter et al., 2019). Epithelia differ in their area and cell shape distributions. We therefore used light-sheet microscopy to determine the apical and basal cell area and cell shape distributions in an E11.5 lung tube (Fig. 7C, D). To reproduce the wide area distributions, we had to introduced a Gaussian distribution for the cell cycle times and the cell division thresholds (Supplementary Table 1) (Kokic et al., 2019).

Shear stress does not directly deform cells, but rather cells sense shear stress via their primary cilium and actively respond with cell shape changes (Galbraith et al., 1998; Weinbaum et al., 2011). However, also this indirect shape change corresponds to a force that the cells generate intracellularly. Accordingly, we represent the effect of shear stress by applying a constant force at the top and bottom of the simulated tissue (Fig. 7A). This results in a uniform force field with uniform relative displacement of cells along the tissue axis (Fig. 7E), as would be expected in case of shear stress. When we apply uniform growth, we find an almost linear increase of the bias in outgrowth with such an external force (Fig. 7E,F). As shear stress is actively sensed and translated by the cells into a change in cell shape (Galbraith et al., 1998), we note, however, that there is not necessarily a linear correspondence between the extracellular shear force and the intracellular force that reshapes the cell. Other force response curves could therefore result from the intracellular regulatory processes that respond to the shear stress.

Between E10.5 and E11.5, the lung tubes elongate twice more than they widen (Fig. 1E) (Tang et al., 2011). We obtain this 2-fold bias in outgrowth with an elongation force of 1 a.u. (Fig. 7F). It has previously been noted that this bias in outgrowth is accompanied by a bias in cell shape and cell division (Tang et al., 2011; Tang et al., 2018). Cell shape and the cell division axis are linked in that cells in the lung epithelium divide perpendicular to their longest axis when their aspect ratios are greater than 1.53 (Tang et al., 2018). With a force of 1 a.u. and cell division perpendicular to the longest axis, the simulations (Fig. 7G, purple diamonds) recapitulate the measured bias in cell division at E10.5 (Fig. 7G, blue squares, (Tang et al., 2011)), as well as our measured cell area and shape variation (Fig. 7C,D). Note that a slightly lower bias in the cell division angles has been reported at E11.5 (Fig. 7G, yellow circles, (Tang et al., 2018)). We also recapitulate the observed impact of additional stretching forces (Tang et al., 2018) on elongating outgrowth (Fig. 7E,F). Finally, we note that the impact of shear stress on elongating outgrowth depends on the mechanical properties of the cells in our simulations (Fig. 7H). In particular, the higher the cortical or line tension, the smaller the bias, and *vice versa*. The changes in the elongation bias in different mutants and pharmacological perturbations may thus also arise via modulation of cortical tension and cell-cell adhesion. Given that such parameter changes can also affect the cell area and shape variability (Fig. S6), we note that the simultaneous recapitulation of the elongation bias (Fig. 7F), and the cell area and shape distributions (Fig. 7C,D) is significant.

bioRxiv preprint doi: https://doi.org/10.1101/2020.06.22.166231; this version posted June 23, 2020. The copyright holder for this preprint (which was not certified by peer review) is the author/funder. All rights reserved. No reuse allowed without permission.

DISCUSSION

The elongation of epithelial tubes is a key developmental process. We combined a quantitative analysis of lung and kidney branching morphogenesis with computational modelling to evaluate candidate mechanisms for the biased elongation of epithelial tubes. We show that biased elongation is an inherent property of these epithelial tubes, and that it does not require contact with the mesenchyme or an external chemotactic gradient. We note that the epithelial tubes are largely collapsed in early lung and kidney development, and find that the fluid flow that has previously been estimated for early lung development (George et al., 2015) could result in shear stress levels that epithelial cells can, in principle, sense with their primary cilium (Weinbaum et al., 2011). We evaluate the impact of shear stress in a cell-based tissue model, and find that shear stress, unlike constricting forces (Stopka et al., 2019), can explain both the observed biased tube elongation and the observed bias in cell division. Shear stress may thus be a more general driver of biased tube elongation beyond its established role in angiogenesis (Davies, 2009; Galbraith et al., 1998; Galie et al., 2014).

Consistent with a role for shear stress in biased lung tube elongation, the bias in cell division and outgrowth is not observed in embryonic lung epithelia that express the constitutively active form KRas^{G12D} (Tang et al., 2011), a mutation that leads to the disruption of the primary cilium (Tape et al., 2016). The cilium is necessary to respond to shear stress because shear stress does not directly deform cells, but rather cells sense shear stress via their primary cilium and actively respond with cell shape changes (Galbraith et al., 1998; Weinbaum et al., 2011). Cells then divide perpendicular to their longest axis (Hertwig, 1884), and the bias in cell shape along the lung tube axis therefore translates into a bias in cell division (Tang et al., 2011; Tang et al., 2018).

Given that shear stress is actively sensed and translated by the cells into a change in cell shape (Galbraith et al., 1998), there is not necessarily a linear correspondence between the extracellular shear force and the intracellular force that reshapes the cell. For the sake of simplicity and given the absence of contrary data, we modelled the effect of shear stress in our cell-based tissue model by applying a force at one tissue border in the direction of the shear stress. The boundary force results in a uniform force field along the tube as would be expected from shear stress. The force results in biased outgrowth in the direction of the force. With a force that lets us quantitatively recapitulate the measured bias in outgrowth, we also quantitatively reproduce the measured distribution in cell division angles as observed in the mouse lung bud (Tang et al., 2011; Tang et al., 2018). Importantly, in the embryonic mouse lung cells, cells only follow this longest-axis rule if the ratio of the longest to the shortest axis is larger than 1.5; otherwise, the cell division axis is set randomly (Tang et al., 2018). We emphasize that we can reproduce the measured elongation bias and the measured distribution of cell division angles only with the line tension and cortical tension parameters that allow us to also recapitulate the measured apical area and cell neighbour distributions. Smaller tension levels result in more elongation and *vice versa*. Accordingly, mutations that change the epithelial cell mechanics or the composition of the extracellular matrix (ECM) would be expected to affect the elongation bias in tube outgrowth. In addition to its effect on the primary cilium, KRas has previously also been linked to changes in cell shape and motility in airway epithelial cells by affecting cortical actin (Fotiadou et al., 2007; Okudela et al., 2009), and the KRas^{G12D} mutation has been found to upregulate multiple ECM components in the pancreatic stroma (Tape et al., 2016).

While biased tube elongation is observed in isolation, independent of the mesenchyme, we find that the mesenchyme affects the strength of this bias. In this way, the mesenchyme can modulate the particular tube shape and thereby the organ-specific branching architecture (Lin et al., 2003). It is not known how the mesenchyme impacts on lung tube elongation. However, several soluble factors that are secreted in the mesenchyme are known to signal in the epithelium and to affect the composition of the ECM (McCulley et al., 2015). Smooth muscles and the peristaltic fluid movement inside the lung tubes that they generate are not necessary for normal lung branching morphogenesis (Young et al., 2020). We can also exclude that the luminal pressure has a significant impact on tube shape. If the flow was to directly mechanically affect the epithelial cells, one would expect both a stretching of the cells in direction of the shear stress and a widening of the tube in response to the local luminal pressure. As flow is the result of a pressure gradient, the circumference of the tubes would then need to be wider with increasing distance from the larynx. This is not the case. Also, branching morphogenesis of cultured lungs is not affected by

bioRxiv preprint doi: https://doi.org/10.1101/2020.06.22.166231; this version posted June 23, 2020. The copyright holder for this preprint (which was not certified by peer review) is the author/funder. All rights reserved. No reuse allowed without permission.

the presence or absence of the trachea. Accordingly, a fluid-structure interaction appears to have no significant impact on lung tube shape.

Shear stress only has the potential to drive biased elongating outgrowth because the epithelial tubes are so narrow in early lung and kidney development. In later stages, tubes are wide and open. The same level of apical shear stress would then require much higher flow rates, and tube growth indeed becomes isotropic. It remains unclear why the tubes collapse in early developmental stages. Mechanical effects that could, in principle, cause the collapse of the tubes would result in the highest mechanical stress levels in the curved parts. Accordingly, neither curvature nor hoop stress (Hamant et al., 2008) could explain the biased uniform outgrowth of the collapsed tubes. We note that staining for actin, a read-out for tension within tissues, is uniform in the closed tubes, suggesting that any stress that may have been generated during the collapse is quickly relaxed away. Going forward it will be important to identify the cause for tube collapse and understand its potential impact in biasing elongating outgrowth.

Similarly, measurements of the fluid velocity are required. In the mouse lung, fluid flow is well visible at E12.5, but the fluid velocity has not been reported (Nelson et al., 2017). In fact, the published estimate of the flow rate ($\dot{V} = 420\ \mu m^3/s$) is largely based on data from species other than the mouse, and later stages of lung development (George et al., 2015). Direct measurements of the flow rate already in the very early stages of lung development will be of key importance to conclusively evaluate the significance of shear stress in biased lung tube elongation. Similar measurements would be of interest in situations where the pressure gradient between the larynx and the pleural space is altered. A microfluidic setup that enhanced the pressure difference between the larynx and the pleural space resulted in enhanced growth, with overall branch shapes appearing largely normal, although the tube shapes were not quantified (Nelson et al., 2017). Surgical occlusion of the trachea appears to mainly enhance branching (Blewett et al., 1996; Nelson et al., 2017; Unbekandt et al., 2008). The branch shapes have not been quantified, but appear shorter, pointing to a reduced elongation bias, which would be consistent with the expected reduced fluid outflow. In analysing shear stress, we assumed a constant inflow, i.e. constant fluid secretion, at the tips. Currently, it is not known whether fluid secretion is indeed restricted to the tips, and how it is affected by the local luminal fluid pressure. Fluid secretion along the entire branch would lead to increasing flow rates and thus shear stress towards the outlet. Also, since the early lung does not yet have a fractal-like architecture with conserved branch volumes in daughter branches (Iber and Menshykau, 2013), fluid flow rates can be expected to change at branch points. All these parameters need to be measured in experiments and compared to the growth behaviour to evaluate the role of shear stress in biased tube elongation.

In summary, by combining quantitative measurements with simulations, we have shown that flow-induced shear stress can, in principle, explain the biased elongating outgrowth of epithelial tubes in early lung and kidney development. Quantitative measurements of the flow velocity are now important to further validate this hypothesis. Moreover, it will be important to understand why the epithelial tubes collapse, and how the mesenchyme modulates the elongation bias.

bioRxiv preprint doi: https://doi.org/10.1101/2020.06.22.166231; this version posted June 23, 2020. The copyright holder for this preprint (which was not certified by peer review) is the author/funder. All rights reserved. No reuse allowed without permission.

MATERIALS AND METHODS:

Ethical Statement

All experiments were performed in accordance with Swiss federal law and the ordinance provided by the Canton Basel-Stadt and approved by the veterinary office of the Canton Basel-Stadt, Switzerland (approval number 2777/26711).

Mouse strains

Mice were housed at the D-BSSE/UniBasel facility under standard chow, water, enrichment, and light/dark cycles.

To infer tissue boundaries and to mark the 3D cell morphology of the epithelium, the following transgenic alleles were used: Shh-cre (Mouse genome informatics: $Shh^{tm1(EGFP/cre)Cjt}$) (Harfe et al., 2004), $ROSA^{mT/mG}$ (mouse genome informatics: $Gt(ROSA)26Sor^{tm4(ACTB-tdTomato,-EGFP)Luo}$)(Muzumdar et al., 2007) and Hoxb7/myr-Venus (mouse genome informatics: Tg(Hoxb7-Venus*)17Cos) (Chi et al., 2009).

The Shh-cre allele was used to drive Cre recombinase-mediated recombination of the $ROSA^{mT/mG}$ allele. As recombined EGFP localizes to the cell membrane, and *Shh* is only expressed in the lung bud epithelium, individual cell morphology could be segmented. To generate a Shh-cre; $ROSA^{mT/mG}$ double-transgenic line, Shh-cre mice heterozygous for the $Shh^{tm1(EGFP/cre)Cjt}$ allele were crossed with homozygous $ROSA^{mT/mG}$ mice. F1 offspring were crossed again to obtain animals that are homozygous for the $ROSA^{mT/mG}$ and heterozygous for the Shh-cre allele ($Shh^{cre/+}$; $ROSA^{mT/mG}$). For the experiments in this study, $Shh^{cre/+}$; $ROSA^{mT/mG}$ males were either crossed with RjOrl:SWISS wild type or $ROSA^{mT/mG}$ females.

To obtain *Shh* knockout embryos, timed matings of $Shh^{cre/+}$; $ROSA^{mT/mG}$ mice were set. A quarter of the collected embryos were homozygous for the Shh-cre allele and therefore did not carry the wild type *Shh* gene. Shh knockout embryos displayed early defects in vertebrate embryonic tissues, including the brain, limbs as well as in lung patterning and branching.

For the kidney explant cultures, homozygous Hoxb7/myr-Venus males were crossed with RjOrl:SWISS wild type females because of higher pregnancy rates and larger litters.

2D organ culture and time-lapse epifluorescence imaging

Pregnant female mice were sacrificed according to institutional guidelines at the desired embryonic stages. All embryos were sorted using a fluorescence stereomicroscope (Leica Microsystems) according to the desired fluorescent reporters. The lungs and metanephric kidneys were dissected in ice-cold PBS and cultured at the liquid-air interface (Grobstein, 1956) using a trans-well membrane culture system supplemented with explant culture medium (DMEM/F12, 10% FBS (Sigma-Aldrich Chemie GmbH; F9665-500ML), 1x GlutaMAX (Life Technologies Europe BV; A1286001), 1x Penicillin-Streptomycin (Roche; 11074440001)). For the FGFR inhibitor lung cultures, the culture medium was supplemented with 3µM or 5µM SU5402 (Sigma-Aldrich, SML0443) before live imaging. For the lung cultures without a trachea, the trachea was cut right below the larynx or above the carina before live imaging.

To investigate the developmental dynamics of isolated lung bud and ureteric bud (UB) epithelia, mesenchymal tissue was enzymatically removed (Fig. 3D). The experimental procedure was adapted from (Nogawa and Ito, 1995; Yuri et al., 2017). Dissected lungs and kidneys were washed in DMEM/F12 and then incubated in 200ng/ml Collagenase/Dispase (Roche, 10269638001) in DMEM/F12 for 10min (kidney) or 12min (lung) in an incubator (37°C 5% CO_2), washed once in DMEM/F12 with 50% FBS and then placed in 100% FBS on ice for 10min to stop the enzymatic reaction. The mesenchyme was removed using tungsten needles. Isolated UBs were embedded in 50% Growth-Factor Reduced Matrigel (GFRMG) (Corning; 354230) and 50% explant culture medium supplemented with 4ng/ml rhGDNF (R&D; 212-GD), 200 ng/ml human FGF-acidic (Peprotech; 100-17A), 200ng/ml murine R-Spondin (Peprotech; 315-32) and 0.2 µM retinoic acid (Sigma-Aldrich; R2625). A 20 µl drop of this mixture was placed on a trans-well filter, and an isolated UB was carefully moved into the drop, with as little medium as possible, and allowed to sink atop of the membrane to largely restrict growth to two dimensions. Supplemented explant culture medium without GFRMG was added to the well, and the plate was placed in an incubator (37°C, 5% CO_2) for at least 2h prior to live imaging. For the pERK staining (Fig. 3), UBs were isolated and cultured as described, however, the filter membrane was omitted and the samples embedded in a hanging drop of 1:1 GFRMG/explant culture medium + growth factors. Isolated lung buds were placed in a 20µl drop of GFRMG in a tissue-culture treated plate (Corning; 3513) solidified upside down (hanging-drop) in an

bioRxiv preprint doi: https://doi.org/10.1101/2020.06.22.166231; this version posted June 23, 2020. The copyright holder for this preprint (which was not certified by peer review) is the author/funder. All rights reserved. No reuse allowed without permission.

incubator (37°C, 5% CO_2) for 20min, then another drop of GFRMG (15 µl) was added on top. After 30-45min, this drop was overlaid with explant culture medium supplemented with 100ng/ml human FGF10 (Peprotech; 100-26), 50ng/ml human FGF-acidic, 50 ng/ml R-Spondin and 2 µM CHIR99021 (Sigma-Aldrich; SML1046).

Automated time-lapse imaging of the cultured explants was performed using a Nikon epifluorescence microscope, which was equipped with an environmental control chamber. A 10x/0.3na Plan Fluor Ph1 DLL objective with 16mm working distance (Nikon; MRH10101) and a 475/28 excitation filter was used to capture GFP or myr-Venus fluorescence in the epithelium, and a 549/15 excitation filter was used to capture RFP fluorescence in the mesenchyme. Images were acquired using a Hamamatsu Orca Flash 4.0 V2 camera at set positions every hour for 48h (SU5402 and trachea cultures) or 60h (all other cultures with medium changes after 48h).

Immunofluorescence, optical clearing and light-sheet imaging

To detect phosphorylated MAP Kinase Erk1 and Erk2 (pERK) (Fig.3) in E12.5 lungs and kidneys and in mesenchyme-free E11.5 UBs cultured for 72h, immunostaining was performed as described in (Menshykau et al., 2019). Mesenchyme-free UB cultures were treated with Corning Cell Recovery Solution (Corning; 354253) for 10min at 4°C to digest the Matrigel prior to fixation. After staining, an additional post-fixation step with 4% paraformaldehyde (PFA) for 20min at 4°C was performed prior to optical clearing to preserve fluorescence. For the actin immunostaining (Fig. 3F,G, Fig. 5B,C), lung samples were pre-blocked (1% BSA, 10% donkey serum (Sigma-Aldrich; D9663), 0.5% Triton-X (Sigma-Aldrich; T8787) in 1x PBS) overnight, incubated with primary antibody diluted 1:200 (Anti-Actin: abcam, ab179467) in blocking solution for two days, washed with PBS during one day, incubated with a fluorescently conjugated secondary antibody diluted 1:500 (Alexa Fluor 555: Invitrogen; A-31572) overnight, and washed with PBS during one day. Samples were post-fixed in 4% PFA for 20min and washed in PBS.

Whole-mount tissue clearing of dissected embryonic explants was performed with the Clear Unobstructed Brain/Body Imaging Cocktails and Computational Analysis (CUBIC) protocol as specified by the authors (Susaki et al., 2015). Clearing times in reagents for decolouring, delipidation, permeation (CUBIC-1), and refractive index (RI) matching (CUBIC-2) were adjusted to maximize clearing efficiency and minimize quenching. Following a 1h fixation in 4% PFA, samples were incubated in 1/2 CUBIC-1 (CUBIC-1:H2O=1:1) for two-four days, and in 1X CUBIC-1 until they became transparent. All samples were subsequently washed several times in PBS. The actin immunostaining was performed after the CUBIC-1 clearing steps. All samples were then treated with 1/2 CUBIC-2 (CUBIC-2:PBS=1:1) for two-four days. Lastly, incubation in 1X CUBIC-2 was done until the desired transparency was achieved. CUBIC-1 steps were performed on a shaker at 37 °C while CUBIC-2 steps at RT. Cleared samples were embedded in 2% low-melting-point solid agarose cylinders, and immersed in CUBIC-2 overnight. 3D image stacks were acquired using a Zeiss Lightsheet Z.1 SPIM microscope using a 20x/1.0 clearing objective.

3D organ culture, mounting, and time-lapse light-sheet imaging

Following dissection in DPBS at RT, all lung explants were cultured in sterile Dulbecco's modified Eagle's medium w/o phenol red (DMEM) (Life Technologies Europe BV; 11039021) containing 10% Fetal Bovine Serum (FBS) (Sigma-Aldrich Chemie GmbH; F9665-500ML), 1% Glutamax (Life Technologies Europe BV; A1286001), and 1% penicillin/streptomycin (Life Technologies Europe BV; 10378-016). All specimens were equilibrated at 37°C with 5% CO_2 in a humidified incubator for 1h.

In the meantime, LMP hollow agarose cylinders were prepared according to (Udan et al., 2014). Hollow cylinders allow for unencumbered 3D embryonic growth, minimize tissue drift, enable imaging from multiple orientations, and allow for better nutrients and gas perfusion. Within a hollow cylinder, a single specimen was suspended in undiluted Matrigel (VWR International GmbH; 734-1101) to recapitulate the in-vivo microenvironment. All cylinders were kept at 37°C with 5% CO_2 in culture media for 1h prior to mounting.

For an overnight culture, the imaging chamber was prepared first by sonication at 80°C and subsequent washes in ethanol and sterile PBS. After the chamber was assembled, culture medium and allowed to equilibrate at 37°C with 5% CO_2 for at least 2h before a cylinder was mounted for imaging. Furthermore, to compensate for evaporation over time and maintain a fresh culture media environment, peristaltic pumps were installed to supply 0.4 ml and extract 0.2 ml of culture medium per hour. Each lung explant was then aligned with the focal plane within the centre of a thin light-sheet to enable fine optical sectioning with

bioRxiv preprint doi: https://doi.org/10.1101/2020.06.22.166231; this version posted June 23, 2020. The copyright holder for this preprint (which was not certified by peer review) is the author/funder. All rights reserved. No reuse allowed without permission.

optimal lateral resolution. For this study, all samples were imaged using a 20x/1.0 Plan-APO water immersion objective.

Segmentation of explant morphology in 3D

Light-sheet datasets were transferred to a remote storage server and processed in a remote workstation (Intel Xeon CPU E5-2650 with 512 GB memory). Deconvolution via Huygens Professional software (SVI) improved overall contrast and resolution while Fiji (ImageJ v1.52t) (Schindelin et al., 2012) was used for accentuating cell membranes, enhancing local contrast, and removing background fluorescence. To extract 3D morphological measurements, the length was measured along the centre of Imaris 9.1.2 (Bitplane, South Windsor, CT, USA) iso-surfaces, and cross-sections of tubular bronchial portions were masked and exported into Fiji, where 2D circumference was calculated and averaged over the tube.

Segmentation and skeletonization of 2D culture datasets

Epifluorescence images of embryonic lung and kidney explants were processed in Fiji (ImageJ v1.52t) (Schindelin et al., 2012). Before segmentation, local image contrast was increased, and image background subtracted. Images were then binarized using a global thresholding method, and boundaries were smoothened by applying a gaussian blur filter. Skeletonization of binarized images was performed with the Skeletonize3D plugin, the coordinates and length of all branches from a given skeleton were inferred with the AnalyzeSkeleton plugin (Arganda-Carreras et al., 2010), and branch widths were measured with the BoneJ plugin (v1.4.2) (Doube et al., 2010) (Supplementary Fig.1.2).

Branch analysis software

Analysing the branching behaviour over time required the generation of branch lineages from a skeletonized time series. To this end, a MATLAB script was created to quantify branch length and width and track all branches over time (see https://gitlab.ethz.ch/chrlang/branching-analysis).

Continuum-mechanical simulations of epithelial tube collapse

A full technical description of the custom finite element simulation framework that we employed to simulate epithelial tube collapse can be found in (Vetter et al., 2013). In brief, the shape of the epithelium was represented by third-order finite beam elements, embedded in a corotational formulation to account for geometrically nonlinear deformations. A second-order predictor-corrector scheme was used to integrate Newton's equations of motion. The simulated elastic energy consisted of the sum of bending, axial compression or extension, and transverse shear. In addition, elastic contact between tube segments was modelled using Hertzian contact mechanics where applicable.

Estimation of shear stress levels in embryonic lungs

The wall shear stress on the apical side of a closed lung tube was estimated with the finite element software Comsol Multiphysics (v5.4). As a reference geometry, we used a section of a lung tube originating from an E11.5 embryo of the $Shh^{cre/+}$ line described above. We chose a 400 μm segment from the carina to the first branch of the left lung lobe (LL1). A surface encompassing the lumen of this tube was extracted from the light-sheet images using the 'automatic surface creation' feature of Imaris. The intense fluorescence in this region imposed us to include, in addition to the apical surface, a part of the tissue surrounding the lumen. Consequently, the geometry obtained had a cross-sectional opening of about 20 μm along its minor axis. To reduce the luminal width back to the measured range, the geometry was scaled down along the Z-axis in Paraview (v5.7.0). Different scaling factors were employed to obtain several versions of this geometry with varying degrees of lumen opening. Fluid flow inside the lumen was simulated by solving the Stokes equations for incompressible Newtonian fluids. The dynamic viscosity of the fluid was set to 0.016 Pa·s (Bokka et al., 2015), and its mass density was set to that of water (1000 kg/m^3). A no-slip condition was assumed at the interface between the fluid and the surface of the epithelium. To generate fluid motion, the flow rate at the inlet was set to 420 $\mu m^3/s$ (George et al., 2015), and the pressure at the outlet was maintained at 1 atm. The average wall shear stress value on the apical surface was measured with a boundary probe.

Cell-based simulations of shear stress effect

We simulated the growth of the lung epithelium subjected to shear stress using a vertex model available in the Chaste framework (Fletcher et al., 2013; Mirams et al., 2013). The dynamics of the vertices were derived

bioRxiv preprint doi: https://doi.org/10.1101/2020.06.22.166231; this version posted June 23, 2020. The copyright holder for this preprint (which was not certified by peer review) is the author/funder. All rights reserved. No reuse allowed without permission.

from the potential energy of the system, as previously proposed (Nagai and Honda, 2009). The parameters used to calibrate the model are given in Supplementary Table 1. The initial tissue configuration was comprised of 100 cells arranged in a honeycomb. While the cells located in between were proliferative, the cells on the top-most and bottom-most layers were differentiated and never underwent mitosis. To simulate the elongating effect of shear stress, external forces were applied to the vertices of the differentiated cells. Since the movement of luminal fluid is unidirectional in lung tubes, external forces were applied in the direction of outgrowth (perpendicular to the top and bottom cell layers). Moreover, these forces were applied with opposite directions for the top and bottom layers, thus generating an elongating effect caused by shear stress. We employed MorphoGraphX to 2.5D segment the apical layer of E11.5 lungs, and extract both the area and number of neighbour distributions (Barbier de Reuille et al., 2015). We observed an apical area coefficient of variation (CV) of 0.6 and a percentage of hexagons of 30%. As these two parameters are dependent on cell growth and division rates (Kokic et al., 2019; Sahlin and Jonsson, 2010), the cell division areas and cell cycle durations were drawn randomly from normal distributions to reproduce equivalent statistics *in-silico* (see Supplementary Table 1). Furthermore, in compliance with Hertwig's rule (Hertwig 1884), the cell division axis at mitosis was set to be the shortest axis through the cell centroid. All simulation durations were set to 48.0 a.u.

Lot numbers

- Anti-Actin antibody: GR206286-25
- Phospho-p44/42 MAPK (Erk1/2) (Thr202/Tyr204) antibody: 15
- SU-5402: 104M4713V
- Recombinant human FGF-acidic: 031207 K1014
- Recombinant human FGF10: 0518162-1 K0518
- Recombinant murine R-Spondin: 0516620 E0516
- Recombinant human GDNF: VQ2517081
- Collagenase/Dispase: 11488501

bioRxiv preprint doi: https://doi.org/10.1101/2020.06.22.166231; this version posted June 23, 2020. The copyright holder for this preprint (which was not certified by peer review) is the author/funder. All rights reserved. No reuse allowed without permission.

AUTHOR CONTRIBUTIONS:

DI conceived the study. HG obtained the light-sheet microscopy data in Figures 1 and 4, and, together with OM, the pERK staining in Figure 3B,C. MD obtained the 3D live imaging data in Figure 4, with support from OM and HG. LC obtained and analysed the lung and kidney culture data in Figures 1 and 2, as well as the staining in Figures 3D,F,G and 5, with support from LK. CL obtained and analysed the lung cultures in Figures 1, 3 and 6. LC and CL wrote a Fiji script for the image processing of the filter cultures. MD and CL wrote a MATLAB script for the 2D analysis of the filter cultures. AS obtained, processed, and analysed the light-sheet microscopy data for Figures 6 and 7. SR developed the Comsol and Chaste simulations, with support from RV. RV developed the continuum mechanics simulations. DI wrote the manuscript, with contributions from RV; HG, SR, LC, CL, RV wrote the Methods section and figure legends; all authors approved the final manuscript.

ACKNOWLEGEMENTS:

This work has been supported through an SNF Sinergia grant to DI. We thank Anna Stopka for preliminary quantifications of the biased lung tube elongation, and Alay Shah for segmenting the basal sides of the lung epithelium in MorphoGraphX. We thank Jamie Davies and May Sallam for advice on the mesenchyme-free kidney culture, especially regarding the growth-factor concentrations.

COMPETING INTERESTS:

None declared.

bioRxiv preprint doi: https://doi.org/10.1101/2020.06.22.166231; this version posted June 23, 2020. The copyright holder for this preprint (which was not certified by peer review) is the author/funder. All rights reserved. No reuse allowed without permission.

REFERENCES:

Arganda-Carreras, I., Fernandez-Gonzalez, R., Munoz-Barrutia, A. and Ortiz-De-Solorzano, C. (2010). 3D reconstruction of histological sections: Application to mammary gland tissue. *Microsc Res Tech* **73**, 1019-1029.

Atsuta, Y. and Takahashi, Y. (2015). FGF8 coordinates tissue elongation and cell epithelialization during early kidney tubulogenesis. *Development* **142**, 2329-2337.

Barbier de Reuille, P., Routier-Kierzkowska, A. L., Kierzkowski, D., Bassel, G. W., Schupbach, T., Tauriello, G., Bajpai, N., Strauss, S., Weber, A., Kiss, A., et al. (2015). MorphoGraphX: A platform for quantifying morphogenesis in 4D. *eLife* **4**, 05864.

Blanc, P., Coste, K., Pouchin, P., Azaïs, J.-M., Blanchon, L., Gallot, D. and Sapin, V. (2012). A role for mesenchyme dynamics in mouse lung branching morphogenesis. *PLoS ONE* **7**, e41643.

Blewett, C. J., Zgleszewski, S. E., Chinoy, M. R., Krummel, T. M. and Cilley, R. E. (1996). Bronchial ligation enhances murine fetal lung development in whole-organ culture. *Journal of pediatric surgery* **31**, 869-877.

Bokka, K. K., Jesudason, E. C., Lozoya, O. A., Guilak, F., Warburton, D. and Lubkin, S. R. (2015). Morphogenetic Implications of Peristalsis-Driven Fluid Flow in the Embryonic Lung. *PLoS One* **10**, e0132015.

Bush, K. T., Vaughn, D. A., Li, X., Rosenfeld, M. G., Rose, D. W., Mendoza, S. A. and Nigam, S. K. (2006). Development and differentiation of the ureteric bud into the ureter in the absence of a kidney collecting system. *Dev Biol* **298**, 571-584.

Chi, X., Michos, O., Shakya, R., Riccio, P., Enomoto, H., Licht, J. D., Asai, N., Takahashi, M., Ohgami, N., Kato, M., et al. (2009). Ret-dependent cell rearrangements in the Wolffian duct epithelium initiate ureteric bud morphogenesis. *Dev Cell* **17**, 199-209.

Ciruna, B., Jenny, A., Lee, D., Mlodzik, M. and Schier, A. F. (2006). Planar cell polarity signalling couples cell division and morphogenesis during neurulation. *Nature* **439**, 220-224.

Davies, P. F. (2009). Hemodynamic shear stress and the endothelium in cardiovascular pathophysiology. *Nature clinical practice. Cardiovascular medicine* **6**, 16-26.

Doube, M., Klosowski, M. M., Arganda-Carreras, I., Cordelieres, F. P., Dougherty, R. P., Jackson, J. S., Schmid, B., Hutchinson, J. R. and Shefelbine, S. J. (2010). BoneJ: Free and extensible bone image analysis in ImageJ. *Bone* **47**, 1076-1079.

Fletcher, A. G., Osborne, J. M., Maini, P. K. and Gavaghan, D. J. (2013). Implementing vertex dynamics models of cell populations in biology within a consistent computational framework. *Prog Biophys Mol Biol* **113**, 299-326.

Flitney, E. W., Kuczmarski, E. R., Adam, S. A. and Goldman, R. D. (2009). Insights into the mechanical properties of epithelial cells: the effects of shear stress on the assembly and remodeling of keratin intermediate filaments. *FASEB J* **23**, 2110-2119.

Fotiadou, P. P., Takahashi, C., Rajabi, H. N. and Ewen, M. E. (2007). Wild-type NRas and KRas perform distinct functions during transformation. *Mol Cell Biol* **27**, 6742-6755.

Galbraith, C. G., Skalak, R. and Chien, S. (1998). Shear stress induces spatial reorganization of the endothelial cell cytoskeleton. *Cell motility and the cytoskeleton* **40**, 317-330.

Galie, P. A., Nguyen, D. H., Choi, C. K., Cohen, D. M., Janmey, P. A. and Chen, C. S. (2014). Fluid shear stress threshold regulates angiogenic sprouting. *Proc Natl Acad Sci U S A* **111**, 7968-7973.

George, U. Z., Bokka, K. K., Warburton, D. and Lubkin, S. R. (2015). Quantifying stretch and secretion in the embryonic lung: Implications for morphogenesis. *Mech Dev* **138 Pt 3**, 356-363.

Ghabrial, A. S. and Krasnow, M. A. (2006). Social interactions among epithelial cells during tracheal branching morphogenesis. *Nature* **441**, 746-749.

Gong, Y., Mo, C. and Fraser, S. E. (2004). Planar cell polarity signalling controls cell division orientation during zebrafish gastrulation. *Nature* **430**, 689-693.

Goodwin, K., Mao, S., Guyomar, T., Miller, E., Radisky, D. C., Kosmrlj, A. and Nelson, C. M. (2019). Smooth muscle differentiation shapes domain branches during mouse lung development. *Development* **146**.

Grobstein, C. (1956). Trans-filter induction of tubules in mouse metanephrogenic mesenchyme. *Exp Cell Res* **10**, 424-440.

Hamant, O., Heisler, M. G., Jonsson, H., Krupinski, P., Uyttewaal, M., Bokov, P., Corson, F., Sahlin, P., Boudaoud, A., Meyerowitz, E. M., et al. (2008). Developmental patterning by mechanical signals in Arabidopsis. *Science* **322**, 1650-1655.

Harfe, B. D., Scherz, P. J., Nissim, S., Tian, H., McMahon, A. P. and Tabin, C. J. (2004). Evidence for an expansion-based temporal Shh gradient in specifying vertebrate digit identities. *Cell* **118**, 517-528.

bioRxiv preprint doi: https://doi.org/10.1101/2020.06.22.166231; this version posted June 23, 2020. The copyright holder for this preprint (which was not certified by peer review) is the author/funder. All rights reserved. No reuse allowed without permission.

Hellmich, H. L., Kos, L., Cho, E. S., Mahon, K. A. and Zimmer, A. (1996). Embryonic expression of glial cell-line derived neurotrophic factor (GDNF) suggests multiple developmental roles in neural differentiation and epithelial-mesenchymal interactions. *Mech Dev* **54**, 95-105.

Hertwig, O. (1884). Das Problem der Befruchtung und der Isotropie des Eies. Eine Theorie der Vererbung. *Jenaische Zeitschrift fur Naturwissenschaft.* **18**, 274.

Hines, E. A., Jones, M. K., Verheyden, J. M., Harvey, J. F. and Sun, X. (2013). Establishment of smooth muscle and cartilage juxtaposition in the developing mouse upper airways. *Proc Natl Acad Sci U S A* **110**, 19444-19449.

Iber, D. and Menshykau, D. (2013). The control of branching morphogenesis. *Open biology* **3**, 130088-130088.

Jesudason, E. C., Smith, N. P., Connell, M. G., Spiller, D. G., White, M. R., Fernig, D. G. and Losty, P. D. (2006). Peristalsis of airway smooth muscle is developmentally regulated and uncoupled from hypoplastic lung growth. *Am J Physiol Lung Cell Mol Physiol* **291**, L559-565.

Kishimoto, K., Tamura, M., Nishita, M., Minami, Y., Yamaoka, A., Abe, T., Shigeta, M. and Morimoto, M. (2018). Synchronized mesenchymal cell polarization and differentiation shape the formation of the murine trachea and esophagus. *Nat Commun* **9**, 2816.

Kokic, M., Iannini, A., Villa Fombuena, G., Casares, F. and Iber, D. (2019). Minimisation of surface energy drives apical epithelial organisation and gives rise to Lewis' law. *bioRxiv*.

Lin, Y., Zhang, S., Tuukkanen, J., Peltoketo, H., Pihlajaniemi, T. and Vainio, S. (2003). Patterning parameters associated with the branching of the ureteric bud regulated by epithelial-mesenchymal interactions. *Int J Dev Biol* **47**, 3-13.

McCulley, D., Wienhold, M. and Sun, X. (2015). The pulmonary mesenchyme directs lung development. *Curr Opin Genet Dev* **32**, 98-105.

Menshykau, D., Blanc, P., Unal, E., Sapin, V. and Iber, D. (2014). An interplay of geometry and signaling enables robust lung branching morphogenesis. *Development* **141**, 4526-4536.

Menshykau, D., Michos, O., Lang, C., Conrad, L., McMahon, A. P. and Iber, D. (2019). Image-based modeling of kidney branching morphogenesis reveals GDNF-RET based Turing-type mechanism and pattern-modulating WNT11 feedback. *Nat Commun* **10**, 239.

Michos, O., Cebrian, C., Hyink, D., Grieshammer, U., Williams, L., D'Agati, V., Licht, J. D., Martin, G. R. and Costantini, F. (2010). Kidney development in the absence of Gdnf and Spry1 requires Fgf10. *PLoS Genet* **6**, e1000809.

Min, H., Danilenko, D. M., Scully, S. A., Bolon, B., Ring, B. D., Tarpley, J. E., DeRose, M. and Simonet, W. S. (1998). Fgf-10 is required for both limb and lung development and exhibits striking functional similarity to Drosophila branchless. *Genes Dev* **12**, 3156-3161.

Mirams, G. R., Arthurs, C. J., Bernabeu, M. O., Bordas, R., Cooper, J., Corrias, A., Davit, Y., Dunn, S.-J., Fletcher, A. G., Harvey, D. G., et al. (2013). Chaste: an open source C++ library for computational physiology and biology. *PLoS Comput Biol* **9**, e1002970.

Molladavoodi, S., Robichaud, M., Wulff, D. and Gorbet, M. (2017). Corneal epithelial cells exposed to shear stress show altered cytoskeleton and migratory behaviour. *PLoS One* **12**, e0178981.

Moore, M. W., Klein, R. D., Fariñas, I., Sauer, H., Armanini, M., Phillips, H., Reichardt, L. F., Ryan, A. M., Carver-Moore, K. and Rosenthal, A. (1996). Renal and neuronal abnormalities in mice lacking GDNF. *Nature* **382**, 76-79.

Muzumdar, M. D., Tasic, B., Miyamichi, K., Li, L. and Luo, L. (2007). A global double-fluorescent Cre reporter mouse. *Genesis* **45**, 593-605.

Nagai, T. and Honda, H. (2009). A dynamic cell model for the formation of epithelial tissues. *Philosophical Magazine B* **81**, 699-719.

Nelson, C. M., Gleghorn, J. P., Pang, M. F., Jaslove, J. M., Goodwin, K., Varner, V. D., Miller, E., Radisky, D. C. and Stone, H. A. (2017). Microfluidic chest cavities reveal that transmural pressure controls the rate of lung development. *Development* **144**, 4328-4335.

Nogawa, H. and Ito, T. (1995). Branching morphogenesis of embryonic mouse lung epithelium in mesenchyme-free culture. *Development* **121**, 1015-1022.

Okudela, K., Yazawa, T., Suzuki, T., Sugimura, H. and Kitamura, H. (2009). Role of 3'-phosphoinositides in oncogenic KRAS-induced modulation of shape and motility of airway epithelial cells. *Pathol Int* **59**, 28-37.

Paine, I., Chauviere, A., Landua, J., Sreekumar, A., Cristini, V., Rosen, J. and Lewis, M. T. (2016). A Geometrically-Constrained Mathematical Model of Mammary Gland Ductal Elongation Reveals Novel Cellular Dynamics within the Terminal End Bud. *PLoS Comput Biol* **12**, e1004839.

Park, W. Y., Miranda, B., Lebeche, D., Hashimoto, G. and Cardoso, W. V. (1998). FGF-10 is a chemotactic factor for distal epithelial buds during lung development. *Dev Biol* **201**, 125-134.

bioRxiv preprint doi: https://doi.org/10.1101/2020.06.22.166231; this version posted June 23, 2020. The copyright holder for this preprint (which was not certified by peer review) is the author/funder. All rights reserved. No reuse allowed without permission.

Pichel, J. G., Shen, L., Sheng, H. Z., Granholm, A. C., Drago, J., Grinberg, A., Lee, E. J., Huang, S. P., Saarma, M., Hoffer, B. J., et al. (1996). Defects in enteric innervation and kidney development in mice lacking GDNF. *Nature* **382**, 73-76.

Resnick, A. and Hopfer, U. (2007). Force-response considerations in ciliary mechanosensation. *Biophys J* **93**, 1380-1390.

Rozen, E. J., Schmidt, H., Dolcet, X., Basson, M. A., Jain, S. and Encinas, M. (2009). Loss of Sprouty1 Rescues Renal Agenesis Caused by Ret Mutation. *J Am Soc Nephrol* **20**, 255-259.

Saburi, S., Hester, I., Fischer, E., Pontoglio, M., Eremina, V., Gessler, M., Quaggin, S. E., Harrison, R., Mount, R. and McNeill, H. (2008). Loss of Fat4 disrupts PCP signaling and oriented cell division and leads to cystic kidney disease. *Nat Genet* **40**, 1010-1015.

Sahlin, P. and Jonsson, H. (2010). A modeling study on how cell division affects properties of epithelial tissues under isotropic growth. *PLoS One* **5**, e11750.

Sakakura, T., Nishizuka, Y. and Dawe, C. J. (1976). Mesenchyme-dependent morphogenesis and epithelium-specific cytodifferentiation in mouse mammary gland. *Science* **194**, 1439-1441.

Sanchez, M. P., Silos-Santiago, I., Frisen, J., He, B., Lira, S. A. and Barbacid, M. (1996). Renal agenesis and the absence of enteric neurons in mice lacking GDNF. *Nature* **382**, 70-73.

Schindelin, J., Arganda-Carreras, I., Frise, E., Kaynig, V., Longair, M., Pietzsch, T., Preibisch, S., Rueden, C., Saalfeld, S., Schmid, B., et al. (2012). Fiji: an open-source platform for biological-image analysis. *Nat Methods* **9**, 676-682.

Schittny, J. C., Miserocchi, G. and Sparrow, M. P. (2000). Spontaneous peristaltic airway contractions propel lung liquid through the bronchial tree of intact and fetal lung explants. *American journal of respiratory cell and molecular biology* **23**, 11-18.

Sekine, K., Ohuchi, H., Fujiwara, M., Yamasaki, M., Yoshizawa, T., Sato, T., Yagishita, N., Matsui, D., Koga, Y., Itoh, N., et al. (1999). Fgf10 is essential for limb and lung formation. *Nat Genet* **21**, 138-141.

Stopka, A., Kokic, M. and Iber, D. (2019). Cell-based simulations of biased epithelial lung growth. *Phys Biol* **17**, 016006.

Susaki, E. A., Tainaka, K., Perrin, D., Yukinaga, H., Kuno, A. and Ueda, H. R. (2015). Advanced CUBIC protocols for whole-brain and whole-body clearing and imaging. *Nat Protoc* **10**, 1709-1727.

Tang, N., Marshall, W. F., McMahon, M., Metzger, R. J. and Martin, G. R. (2011). Control of mitotic spindle angle by the RAS-regulated ERK1/2 pathway determines lung tube shape. *Science* **333**, 342-345.

Tang, Z., Hu, Y., Wang, Z., Jiang, K., Zhan, C., Marshall, W. F. and Tang, N. (2018). Mechanical Forces Program the Orientation of Cell Division during Airway Tube Morphogenesis. *Dev Cell*.

Tape, C. J., Ling, S., Dimitriadi, M., McMahon, K. M., Worboys, J. D., Leong, H. S., Norrie, I. C., Miller, C. J., Poulogiannis, G., Lauffenburger, D. A., et al. (2016). Oncogenic KRAS Regulates Tumor Cell Signaling via Stromal Reciprocation. *Cell* **165**, 910-920.

Udan, R. S., Piazza, V. G., Hsu, C.-W., Hadjantonakis, A.-K. and Dickinson, M. E. (2014). Quantitative imaging of cell dynamics in mouse embryos using light-sheet microscopy. *Development* **141**, 4406-4414.

Unbekandt, M., del Moral, P.-M., Sala, F. G., Bellusci, S., Warburton, D. and Fleury, V. (2008). Tracheal occlusion increases the rate of epithelial branching of embryonic mouse lung via the FGF10-FGFR2b-Sprouty2 pathway. *Mech Dev* **125**, 314-324.

Vetter, R., Kokic, M., Gomez, H., Hodel, L., Gjeta, B., Iannini, A., Villa-Fombuena, G., Casares, F. and Iber, D. (2019). Aboave-Weaire's law in epithelia results from an angle constraint in contiguous polygonal lattices. *bioRxiv*.

Vetter, R., Wittel, F. K., Stoop, N. and Herrmann, H. J. (2013). Finite element simulation of dense wire packings. *European Journal of Mechanics - A/Solids* **37**, 160-171.

Weinbaum, S., Duan, Y., Thi, M. M. and You, L. (2011). An Integrative Review of Mechanotransduction in Endothelial, Epithelial (Renal) and Dendritic Cells (Osteocytes). *Cell Mol Bioeng* **4**, 510-537.

Yates, L. L., Schnatwinkel, C., Murdoch, J. N., Bogani, D., Formstone, C. J., Townsend, S., Greenfield, A., Niswander, L. A. and Dean, C. H. (2010). The PCP genes Celsr1 and Vangl2 are required for normal lung branching morphogenesis. *Hum Mol Genet* **19**, 2251-2267.

Young, R. E., Jones, M. K., Hines, E. A., Li, R., Luo, Y., Shi, W., Verheyden, J. M. and Sun, X. (2020). Smooth Muscle Differentiation Is Essential for Airway Size, Tracheal Cartilage Segmentation, but Dispensable for Epithelial Branching. *Dev Cell*.

Yuri, S., Nishikawa, M., Yanagawa, N., Jo, O. D. and Yanagawa, N. (2017). In Vitro Propagation and Branching Morphogenesis from Single Ureteric Bud Cells. *Stem Cell Rep* **8**, 401-416.

bioRxiv preprint doi: https://doi.org/10.1101/2020.06.22.166231; this version posted June 23, 2020. The copyright holder for this preprint (which was not certified by peer review) is the author/funder. All rights reserved. No reuse allowed without permission.

FIGURES & LEGENDS

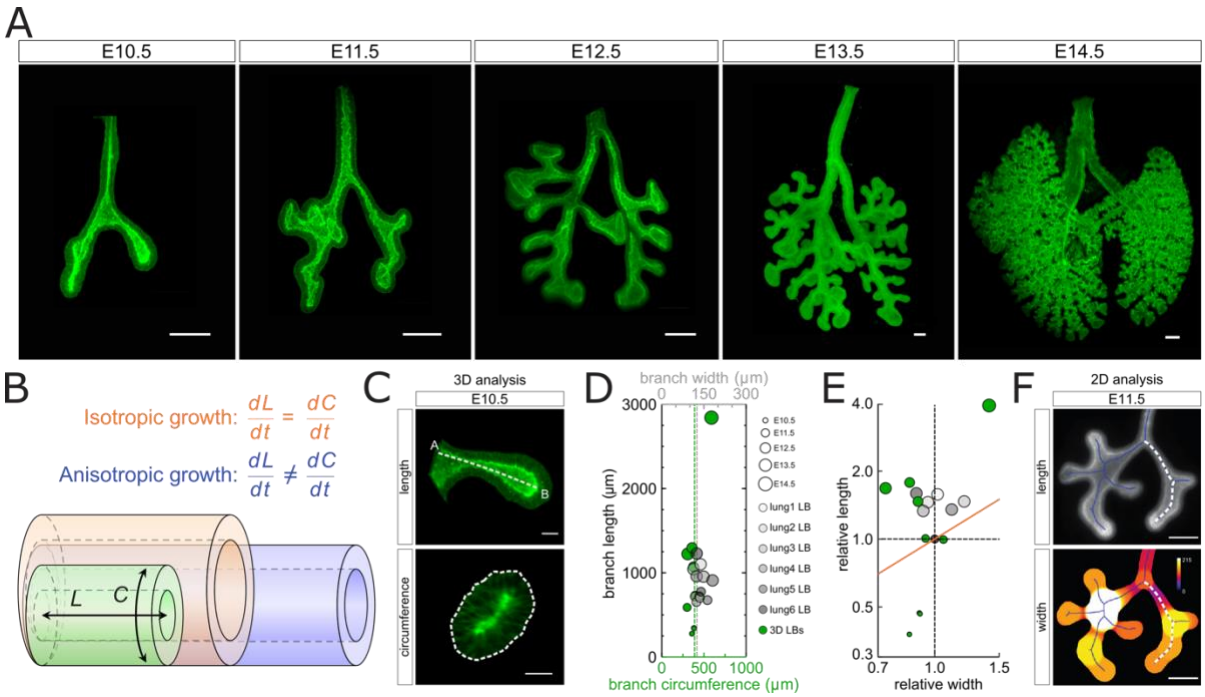

Figure 1. Biased epithelial lung tube elongation

(A) Developmental timeline of serial dissections from mouse embryonic lungs expressing the Shh$^{GC/+}$; ROSA$^{mT/mG}$ reporter (green epithelium, and red mesenchyme) imaged using light-sheet microscopy. Scale bars 200 µm.

(B) Schematic of isotropic and anisotropic tube expansion during development.

(C) 3D morphometric measurements of epithelial tube length and circumference for an E10.5 left bronchus. Scale bars 50 µm.

(D) 3D length and average circumference measurements of the left bronchus of embryonic lungs (E10.5-E14.5 in green), and 2D length and diameter measurements for E11.5 lungs cultured on a filter over 48h (grey). Dot size increases with the developmental stage.

(E) Relative width and length for 3D serial dissections (green) and 2D filter-cultured lungs (grey), normalised to their average size at E11.5. Between E10.5 and E11.5 there is roughly 2-fold more lengthening than widening. After E11.5, data points remain above the orange line, implying that branches continue to elongate more than they widen (anisotropic elongation). Between E13.5 and E14.5, expansion is roughly isotropic.

(F) 2D morphometric measurements of length and diameter for a filter-cultured E11.5 lung. Width scale (colour bar) in µm. Scale bars 200 µm.

bioRxiv preprint doi: https://doi.org/10.1101/2020.06.22.166231; this version posted June 23, 2020. The copyright holder for this preprint (which was not certified by peer review) is the author/funder. All rights reserved. No reuse allowed without permission.

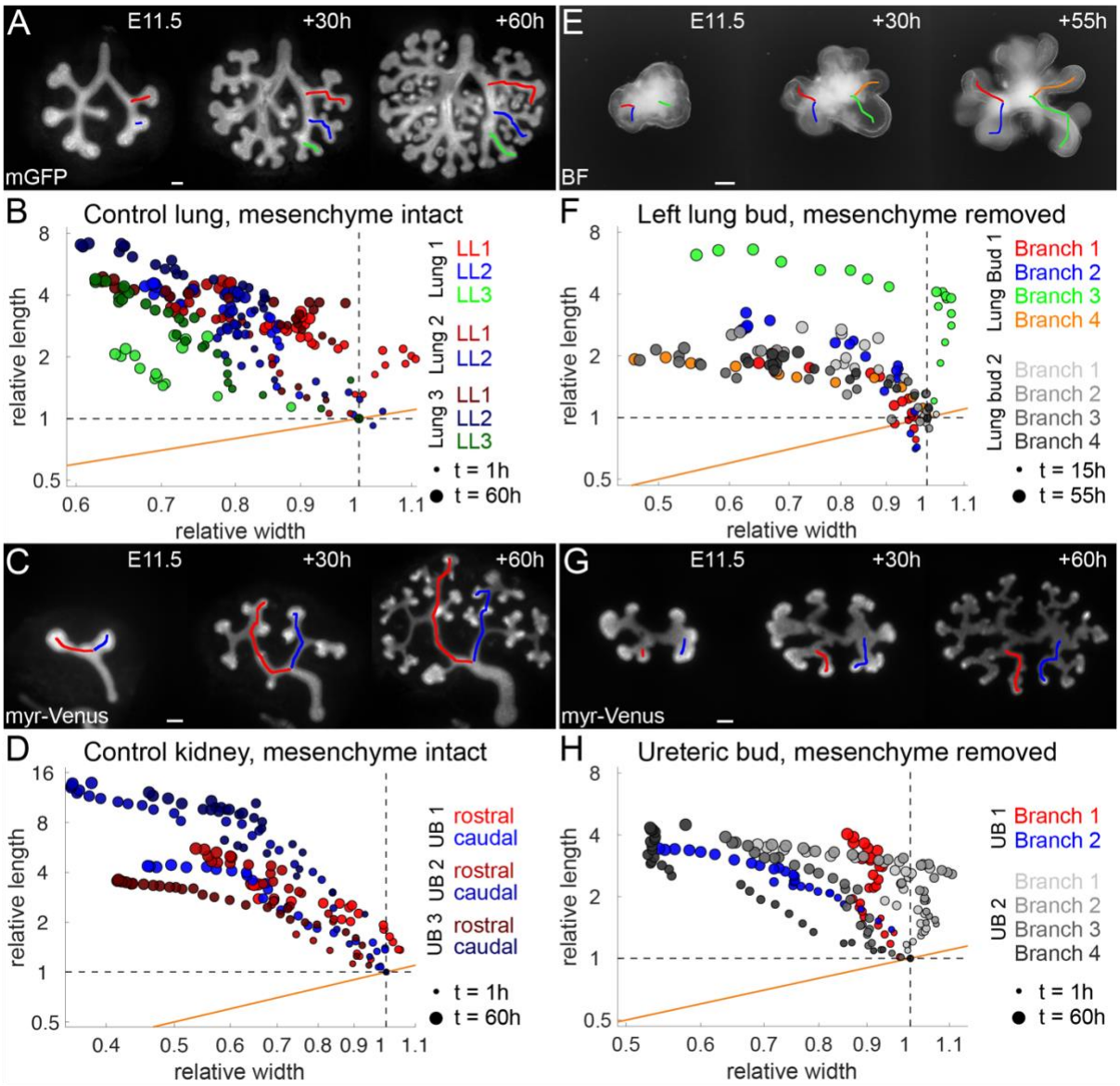

Figure 2. Mesenchyme is not required for biased epithelial tube elongation during lung and kidney development

(A, C, E, G) Epifluorescence/brightfield (inverted) microscopy images of the lung and kidney epithelium expressing mGFP or myr-Venus, respectively, and cultured for up to 60h. Coloured lines mark the branches analysed in (B, D, F, H), respectively. Scale bars 100 µm. **(B, D, F, H)** Relative width and length measurements of lung and kidney epithelial branches. Data points above and away from the orange line show biased tube elongation, meaning branches elongate more than they widen. Dot size increases with culture time.

(A) A representative control lung with intact mesenchyme.

(B) LL1, LL2, and LL3 lung branches show biased epithelial tube elongation (sample n=3; branch n=8).

(C) A representative control kidney with intact mesenchyme.

(D) The rostral and caudal branches of the ureteric bud's (UB) T-shape stage show a bias in tube elongation in control kidneys with intact mesenchyme (sample n=3; branch n=6).

(E) A representative left lung bud epithelium without mesenchyme.

(F) Without mesenchyme, lung branches continue to show biased elongation (sample n=2; branch n=8). The plotted time frame ranges from +15h until +55h, during which branches elongate (See Video S3).

(G) A representative UB epithelium without mesenchyme.

(H) Without mesenchyme, UB branches continue to show biased tube elongation. Compared to the control in (D), branches show a lesser relative increase in length and reduced branch thinning (sample n=3; branch n=6).

bioRxiv preprint doi: https://doi.org/10.1101/2020.06.22.166231; this version posted June 23, 2020. The copyright holder for this preprint (which was not certified by peer review) is the author/funder. All rights reserved. No reuse allowed without permission.

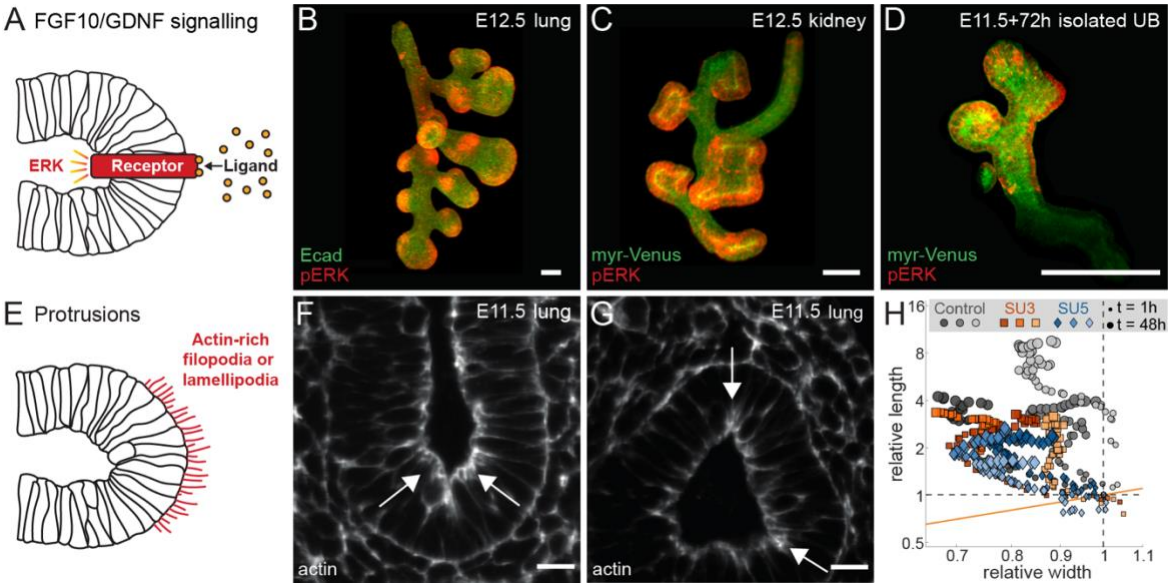

Figure 3. Biased outgrowth is not the result of FGF signalling at the tip

(A) Concentrated growth factor signalling might lead to biased outgrowth.

(**B-D)** pERK antibody staining shows localized spots at the tips of **(B)** an E12.5 embryonic lung, **(C)** an E12.5 kidney, and **(D)** a cultured isolated ureteric bud (UB). Scale bars 100 μm.

(E) A pulling force due to cytoskeletal protrusions could drive biased outgrowth.

(F,G) Actin staining of E11.5 embryonic lungs shows enrichment at the apical, but not at the basal tissue boundary. Scale bars 20 μm.

(H) Relative width and length measurements for the first secondary branch of the left lobe (LL1) of E11.5 control (Ctrl, circles) and FGFR inhibitor-treated (SU3 = SU5402 3uM (squares), SU5 = SU5402 5uM (diamonds)) lungs over 48h. Different colour shades distinguish the data for different lung samples (n = 3 for each condition). Treatment with SU5402 results in more thinning and thus a stronger elongation bias of secondary branches.

bioRxiv preprint doi: https://doi.org/10.1101/2020.06.22.166231; this version posted June 23, 2020. The copyright holder for this preprint (which was not certified by peer review) is the author/funder. All rights reserved. No reuse allowed without permission.

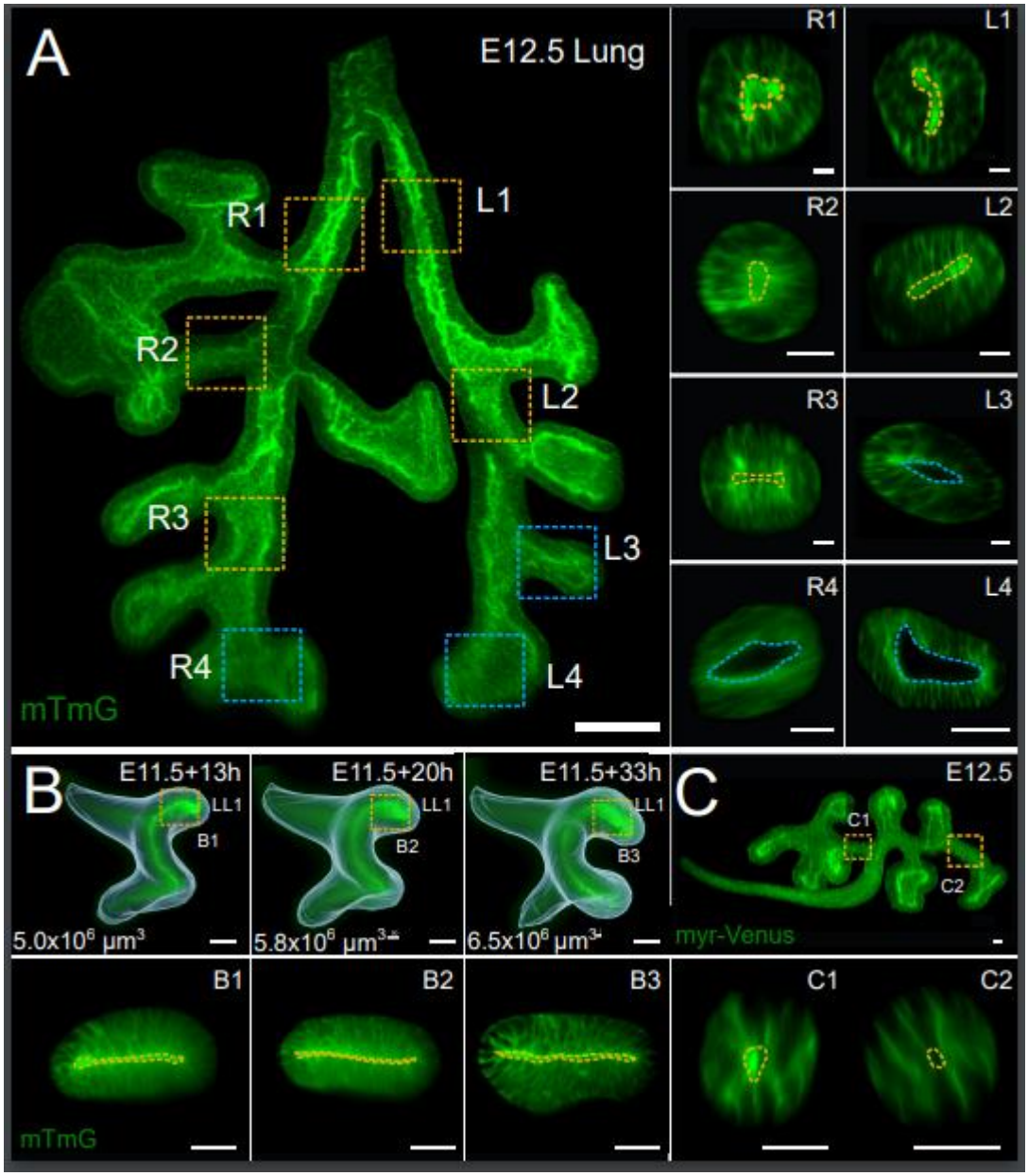

Figure 4. Collapsed epithelial tubes in embryonic mouse lungs and kidneys

(A) Light-sheet fluorescence microscopy image of CUBIC-cleared embryonic lung. Dotted boxes mark different regions in the branching tree where luminal morphology was analysed. Cross-sections illustrate elliptical tissue shapes with narrow luminal spaces in tubular sections (yellow outlines), as well as wider luminal spaces in tips and branch points (blue outlines). Scale bars 50 µm.

(B) High-resolution light-sheet microscopy time-lapse imaging of embryonic lung development. Iso-surface overlays highlight shape changes and volume increase over time. Cross-sections in boxed regions (lower panels) corroborate dynamic collapsed morphologies in elongating epithelial tubes (yellow outlines). The specimen was imaged for over 40h every 20min. Scale bars 50 µm.

(C) Embryonic kidney epithelia also display narrowed tubular architectures (yellow outlines). Scale bars 25 µm.

bioRxiv preprint doi: https://doi.org/10.1101/2020.06.22.166231; this version posted June 23, 2020. The copyright holder for this preprint (which was not certified by peer review) is the author/funder. All rights reserved. No reuse allowed without permission.

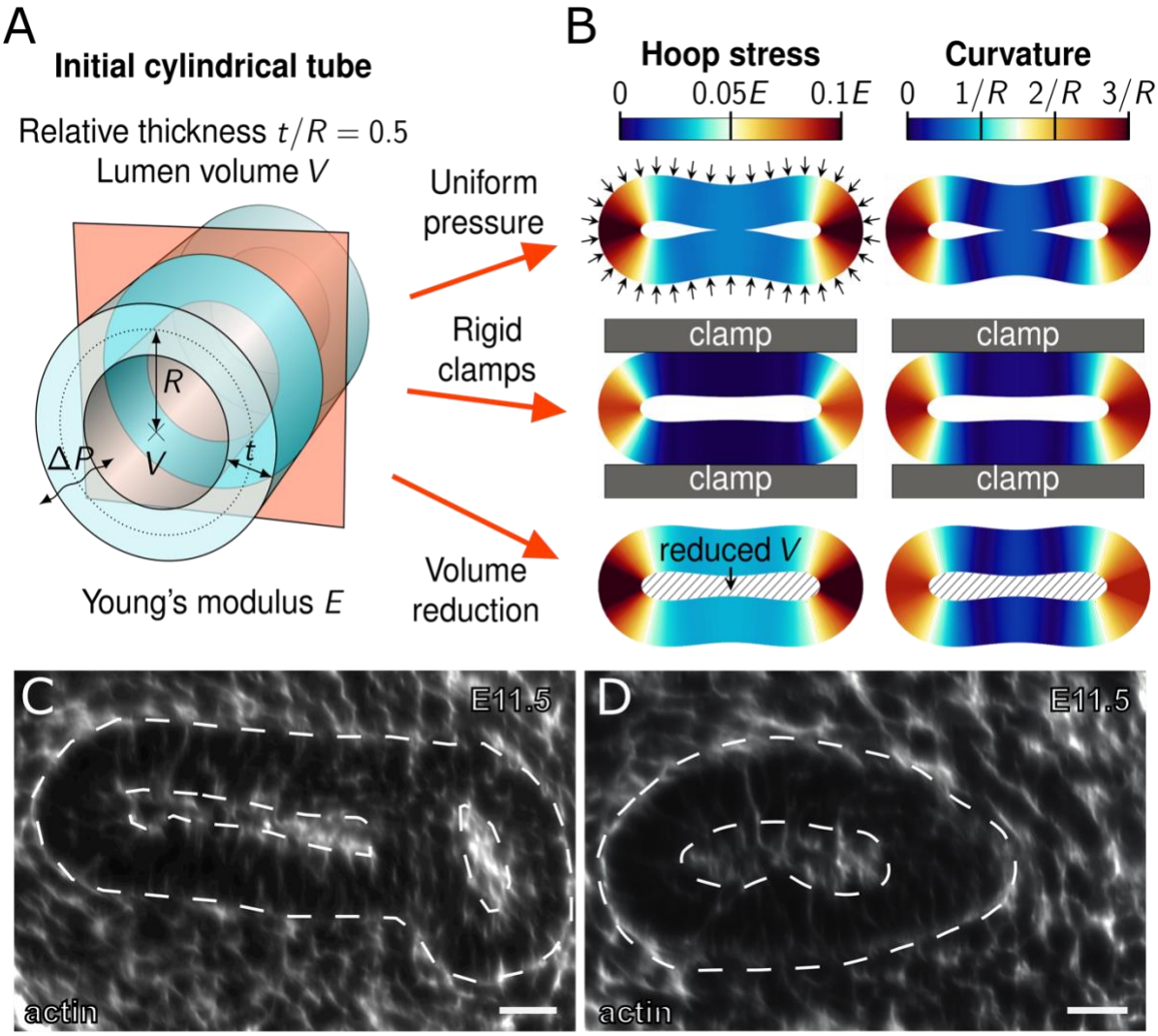

Figure 5. Mechanically forced tube collapse does not result in directional cues for uniform biased outgrowth

(A,B) Mechanical finite element simulations of collapsing epithelial tubes.

(A) Schematic of the initial tubular configuration. A two-dimensional cross-section (red) was simulated using linear viscoelasticity.

(B) Resulting collapsed shapes for three different scenarios: a uniform pressure difference ΔP (top row, arrows), rigid external clamps (middle row, grey bars), and a reduced lumen volume V (bottom row, hatched area). Colours indicate the measured hoop stress (left column) in units of Young's modulus E, and the midline curvature (right column) in units of the inverse initial tube radius, $1/R$. Hoop stress is localised almost exclusively in the highly curved extremal regions.

(C,D) Actin staining is higher at the apical side, but otherwise uniform in cross-sections of closed epithelial tubes from an E11.5 mouse lung. Scale bars 30 μm.

bioRxiv preprint doi: https://doi.org/10.1101/2020.06.22.166231; this version posted June 23, 2020. The copyright holder for this preprint (which was not certified by peer review) is the author/funder. All rights reserved. No reuse allowed without permission.

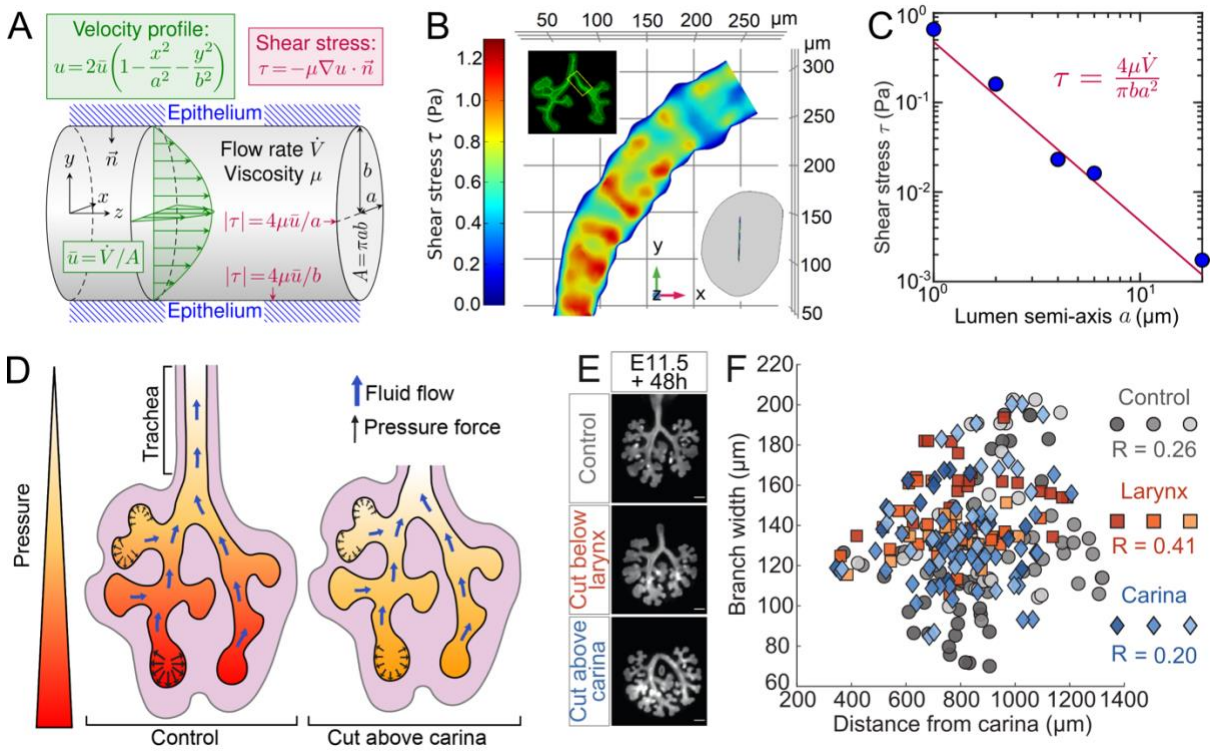

Figure 6. Shear stress in the developing lung

(A) Schematic of shear stress for Hagen-Poiseuille flow in a tubular lumen with elliptical cross section. Wall shear stress $|\tau|$ is maximal in weakly curved regions (minor ellipse axis) and minimal in strongly curved regions (major ellipse axis) of the luminal surface.

(B) Estimated wall shear stress levels at the apical surface of a 400 µm epithelial tube segment that was extracted between the carina and the first branch of the left lung lobe (LL1) (inset). The lumen geometry after numerical rescaling had an average cross sectional opening of 2 µm.

(C) The lumen geometry presented in Fig 6B was rescaled with different scaling factors. For each factor employed, the lumen semi-axis a, and the average wall shear stress on the apical surface τ were determined (blue dots). The average level of wall shear stress on the apical surface can be well approximated from a Hagen-Poiseuille flow profile in an elliptical tube of equivalent size (red line).

(D) Fluid secreted by the cells at the bud tips flows toward the trachea opening. For such a flow to exist, the fluid pressure must be higher at the tips than at the trachea opening. In the case of a FSI, the luminal fluid pressure would widen the branches at the tips more than the branches near the trachea. The existence of such FSI can be tested by reducing the pressure difference between the tips and the outlet. This was achieved by culturing the lungs without their trachea.

(E) Epifluorescence microscopy images of E11.5 lung epithelium, expressing mGFP, after culture on a filter for 48h. The distance of the branches from the tracheal opening was altered by cutting the trachea either below the larynx or above the carina prior to the culture. Control lungs maintained an intact trachea. Scale bars 200 µm.

(F) Branch width and distance measurements for all branches of the left lobe of the lung cultures in (E) at the culture endpoint. Different symbol types mark the different culture conditions regarding trachea length. Different colour shades distinguish the data for different lung samples (n = 3 for each condition). Branch width does not depend on the distance from the tracheal opening, reflected by low Pearson correlation coefficients R.

bioRxiv preprint doi: https://doi.org/10.1101/2020.06.22.166231; this version posted June 23, 2020. The copyright holder for this preprint (which was not certified by peer review) is the author/funder. All rights reserved. No reuse allowed without permission.

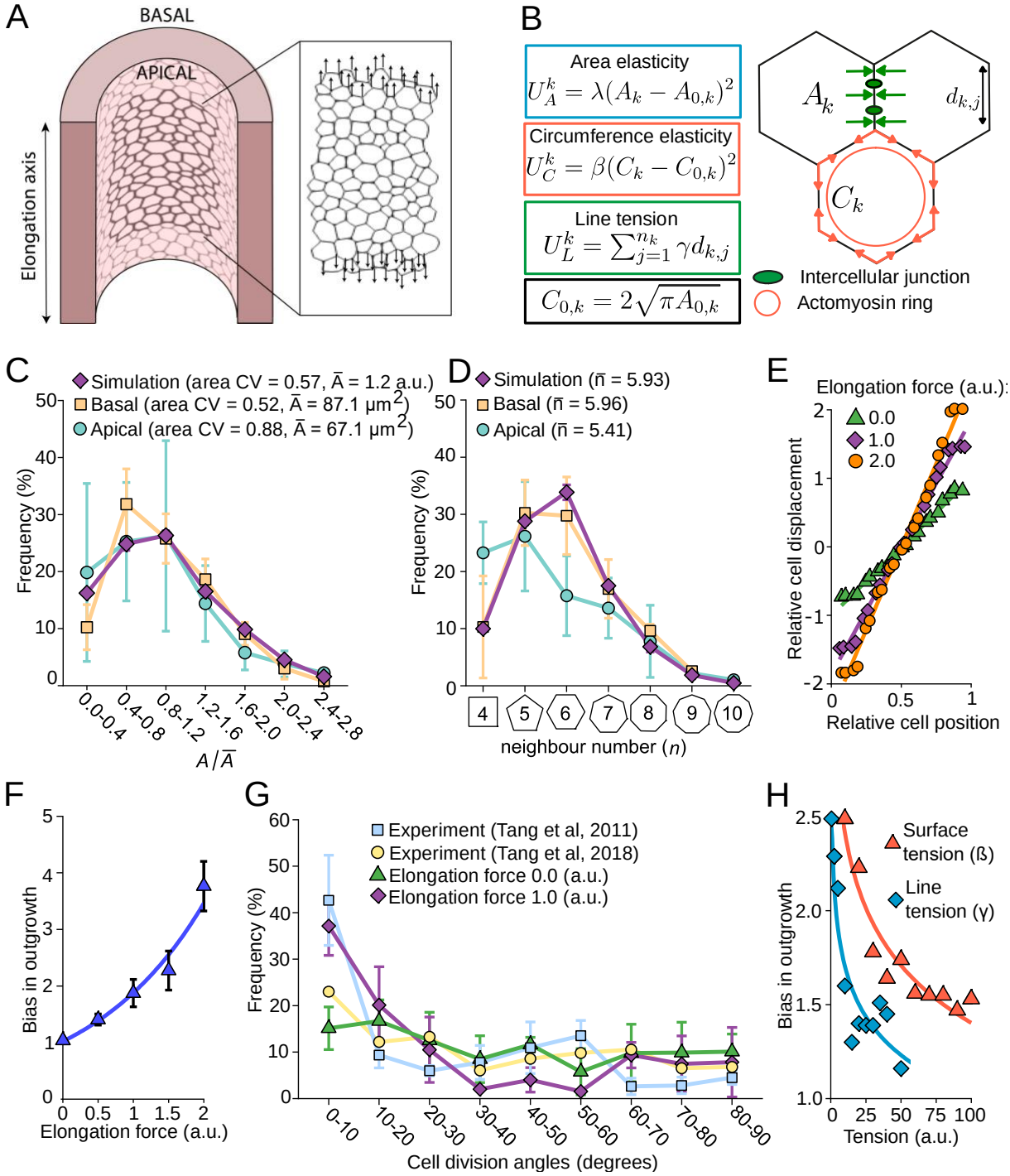

Figure 7. Shear stress forces can result in the observed bias in cell shape and outgrowth

(A) The apical surface of the lung epithelium was simulated with a 2D vertex model. The elongating effect of shear stress was reproduced by applying external forces to the vertices of the cells at the top-most and bottom-most layers of the tissue.

(B) Schematic of the cell-based model. The potential energy of the system is comprised of three contributions. The area elasticity energy U_A penalizes any deviation of the cell area A_k from its target area $A_{0,k}$. The constant λ defines how resistant the cells are to deformations. Similarly, the circumference elasticity energy U_C aims to emulate the contractility of the actomyosin ring by penalizing any deviation of the cell circumference C_k from its target circumference $C_{0,k}$. The line tension U_L energy gives rise to a force associated with cell-cell adhesion. Low values of γ characterize stable and favourable contacts between cells.

bioRxiv preprint doi: https://doi.org/10.1101/2020.06.22.166231; this version posted June 23, 2020. The copyright holder for this preprint (which was not certified by peer review) is the author/funder. All rights reserved. No reuse allowed without permission.

(C,D) The cell area (C) and cell shape (D) distributions of E11.5 lung epithelial cells were measured at their apical (green) and basal (yellow) sides. All parameters in the vertex model (purple) were set so that simulated tissues reproduce the measured distributions (n = 3 for experimental tissues and n = 5 for simulated tissues, error bars show standard deviations).
(E) Relative displacement of the cells as a function of their initial positions in the simulated tissues. Regardless of the magnitude of the elongation force applied, the cells are displaced uniformly along the tissue axis during the simulations.
(F) Bias in outgrowth of the simulated tissues as a function of the elongation forces applied. A force of 1.0 a.u. yields the measured (Tang et al., 2011; Tang et al., 2018) 2-fold elongation bias of lung tubes (n = 5, error bars show standard deviations).
(G) Distribution of the cell division angles in the simulated tissues in the presence or absence of an elongation force. The elongation force 1.0 a.u. yields a bias in cell division orientation equivalent to the bias reported by (Tang et al., 2011); n = 5 for simulated tissues, error bars show standard deviations.
(H) Bias in outgrowth of tissues subjected to an elongation force of 1.5 a.u. as a function of their surface tensions or line tensions. High cortical tensions result in reduced biased outgrowth.

bioRxiv preprint doi: https://doi.org/10.1101/2020.06.22.166231; this version posted June 23, 2020. The copyright holder for this preprint (which was not certified by peer review) is the author/funder. All rights reserved. No reuse allowed without permission.

SUPPLEMENTARY TABLES:

Supplementary Table 1: Parameter values used in the Chaste simulations.

Parameter	Description	Value	Dimension	Reference
η	Drag coefficient	1.0	Time $(\text{Length})^{-1}$	(Fletcher et al. 2013)
λ	Area deformation energy coefficient	100	Force $(\text{Length})^{-3}$	(Fletcher et al. 2013)
β	Membrane surface energy coefficient	10	Force $(\text{Length})^{-1}$	(Fletcher et al. 2013)
γ	Cell-cell adhesion energy coefficient	0,5	Force	(Fletcher et al. 2013)
T cycle	Cell cycle duration	N(12, 7.2)	Time	Figure 7 C,D
Ad	Area division threshold	N(1.5, 0.9)	Length^2	Figure 7 C,D
Dt	Timestep	0.002	Time	(Fletcher et al. 2013)
d min	Cell rearrangement threshold	0.01	Length	(Fletcher et al. 2013)

bioRxiv preprint doi: https://doi.org/10.1101/2020.06.22.166231; this version posted June 23, 2020. The copyright holder for this preprint (which was not certified by peer review) is the author/funder. All rights reserved. No reuse allowed without permission.

SUPPLEMENTARY FIGURES

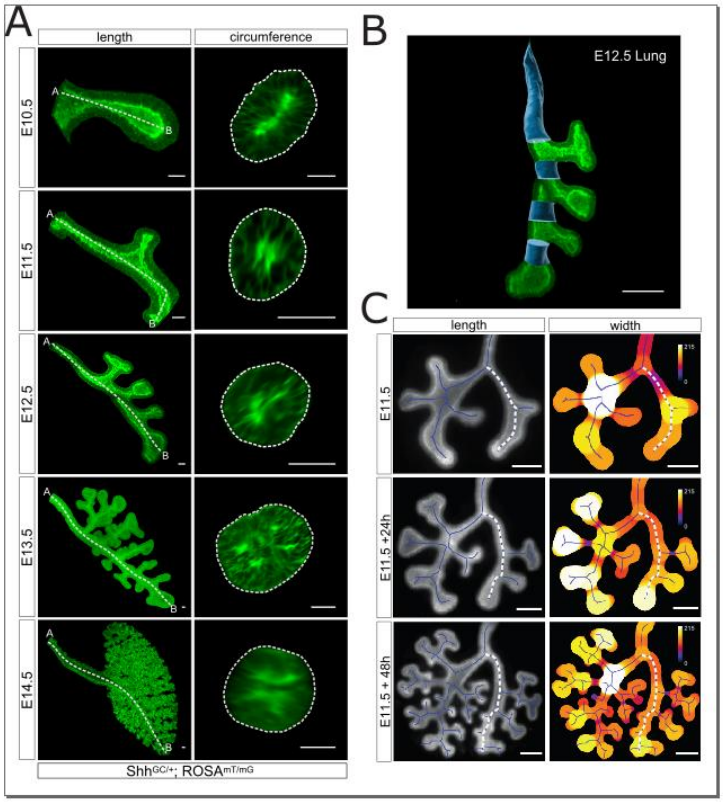

Supplementary Figure 1: Measuring epithelial morphology in growing epithelial tubes
(A) 3D morphometric measurements of branch length and average circumference for a developmental timeline of a mouse lung. Specimens were serially isolated between E10.5 and E14.5 and carried the Shh$_{GC/+}$; ROSA$_{mT/mG}$ reporter, which enabled the visualization of the embryonic epithelium. Branch length was measured from below the carina to the most distal tip, while average branch circumference was calculated for tubular cross-sections. Scale bars 50 µm. **(B)** E12.5 mouse lung with iso-surface overlays denoting tubular sections used for morphometric quantifications (blue). Scale bar 200 µm. **(C)** 2D morphometric measurements of length and diameter for an E11.5 lung cultured on a filter for 48h. Width scale in µm. Scale bars 200 µm.

bioRxiv preprint doi: https://doi.org/10.1101/2020.06.22.166231; this version posted June 23, 2020. The copyright holder for this preprint (which was not certified by peer review) is the author/funder. All rights reserved. No reuse allowed without permission.

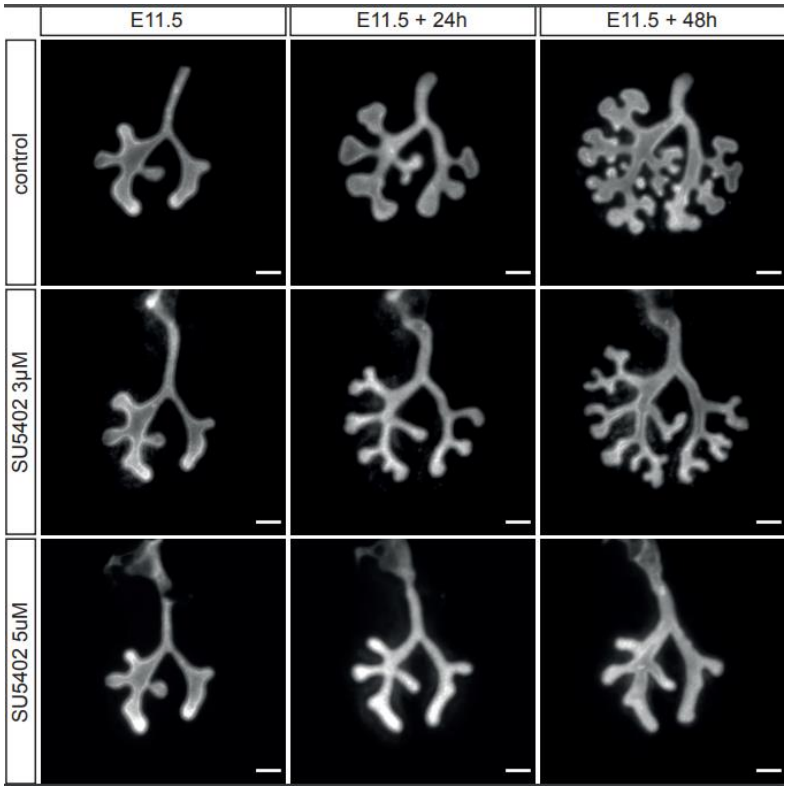

Supplementary Figure 2: SU5402 timelapse cultures
Culture of E11.5 embryonic lungs under control conditions and under different concentrations of the FGFR inhibitor SU5402 at different concentrations for 48h. Treatment with SU5402 does not reduce the elongation of secondary branches. Scale bars 200 µm.

bioRxiv preprint doi: https://doi.org/10.1101/2020.06.22.166231; this version posted June 23, 2020. The copyright holder for this preprint (which was not certified by peer review) is the author/funder. All rights reserved. No reuse allowed without permission.

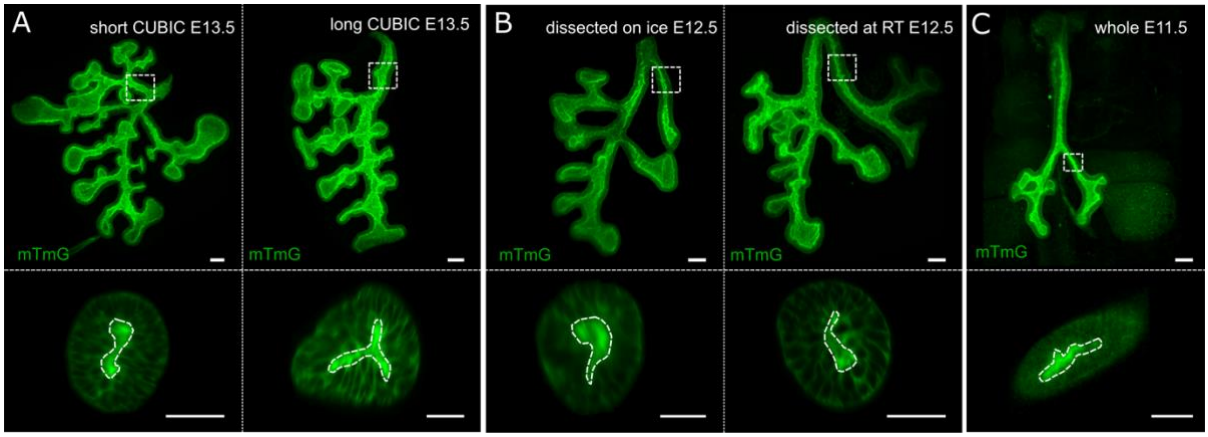

Supplementary Figure 3. Narrow luminal spaces are not the result of dissection /clearing conditions

3D rendering of mouse lung explants (top) and cross-sectional slices (bottom) of specimens **(A)** cleared using a short CUBIC regimen (2 days in reagent-1, 2 days in reagent-2) and a long CUBIC regimen (4 days in reagent-1, 4 days in reagent-2) displaying narrow luminal spaces. Similarly, **(B)** both explants dissected on ice and at room temperature (RT), and cleared using a short CUBIC regimen, also showed collapsed lumens. Furthermore, the same luminal morphology was observed in **(C)** CUBIC cleared whole-embryos imaged through thoracic cavity. Scale bars 100 μm.

bioRxiv preprint doi: https://doi.org/10.1101/2020.06.22.166231; this version posted June 23, 2020. The copyright holder for this preprint (which was not certified by peer review) is the author/funder. All rights reserved. No reuse allowed without permission.

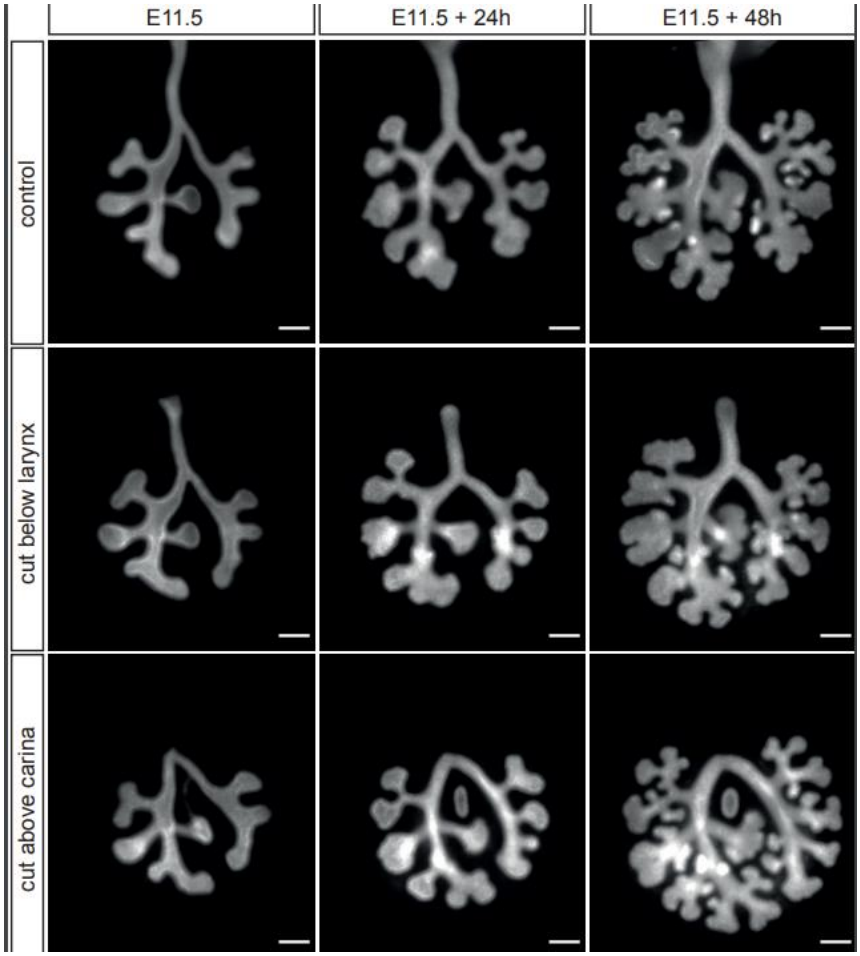

Supplementary Figure 4: Timelapse cultures of lungs with intact and cut trachea
Culture of E11.5 embryonic lungs with intact trachea as control condition and with tracheas either cut below the larynx or above the carina for 48h. Altering the tracheal length does not impact on branching morphogenesis. Scale bars 200 m.

bioRxiv preprint doi: https://doi.org/10.1101/2020.06.22.166231; this version posted June 23, 2020. The copyright holder for this preprint (which was not certified by peer review) is the author/funder. All rights reserved. No reuse allowed without permission.

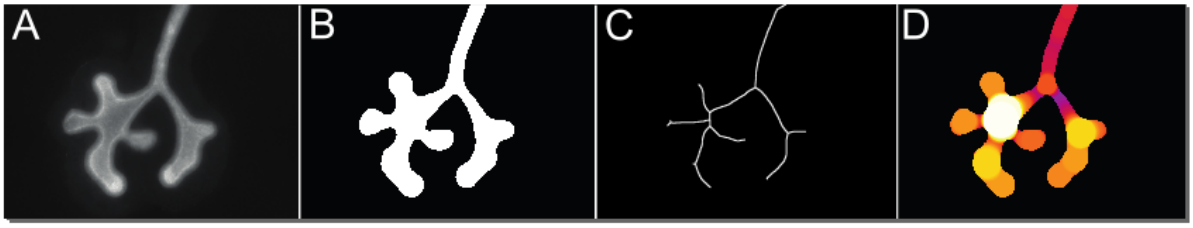

Supplementary Figure 5: Image segmentation and skeletonization
Segmentation of raw images **(A)** resulted in binary images **(B),** which were then used to generate skeletons (**C**, inverted for illustration purposes). Thickness map images **(D)** were generated with the Fiji plugin BoneJ to infer branch widths.

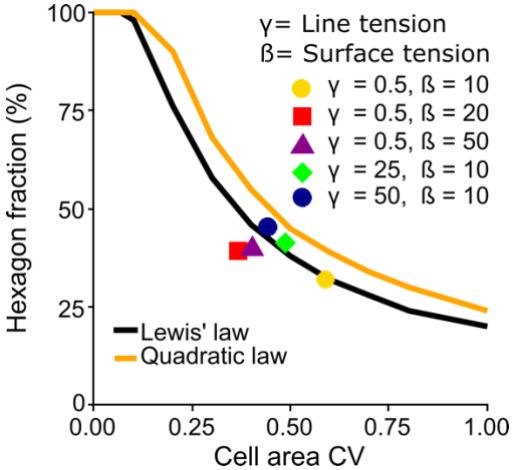

Supplementary Figure 6: Impact of parameter variations in the Chaste simulations
Impact of the membrane surface energy β and the cell-cell adhesion energy γ on the hexagon fraction and area CV in the Chaste simulations. As expected for a tissue representation of epithelia, the simulations reproduce the relationship between the hexagon fraction and the cell area CV as predicted based on Lewis' law (black) or the quadratic law (yellow line) (Kokic et al., 2019).

bioRxiv preprint doi: https://doi.org/10.1101/2020.06.22.166231; this version posted June 23, 2020. The copyright holder for this preprint (which was not certified by peer review) is the author/funder. All rights reserved. No reuse allowed without permission.

SUPPLEMENTARY VIDEOS

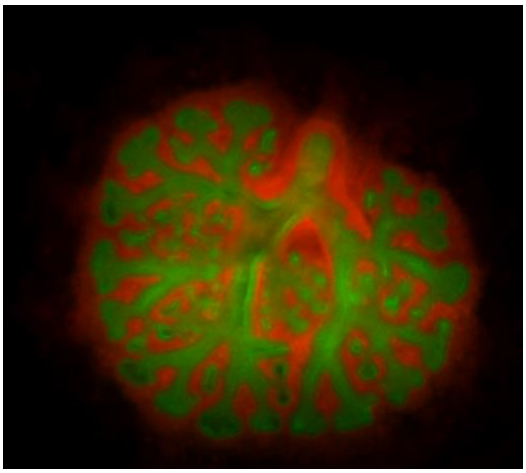

Supplementary Video 1: Lung explant culture
Time-lapse movie of a Shh$^{GC/+}$; ROSA$^{mT/mG}$ E11.5 lung cultured for 60h. Mesenchyme shown in red, *Shh*-expressing epithelium in green. (AVI 6.4 MB).

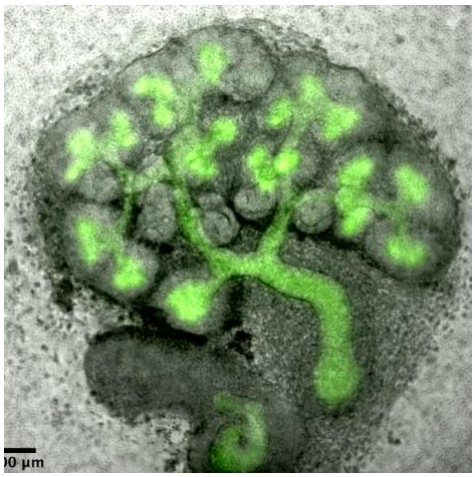

Supplementary Video 2: Kidney explant culture
Time-lapse movie of an E11.5 kidney cultured for 60h. HoxB7/myr-Venus expression is shown in green, brightfield in grey. (AVI 18.7 MB)

bioRxiv preprint doi: https://doi.org/10.1101/2020.06.22.166231; this version posted June 23, 2020. The copyright holder for this preprint (which was not certified by peer review) is the author/funder. All rights reserved. No reuse allowed without permission.

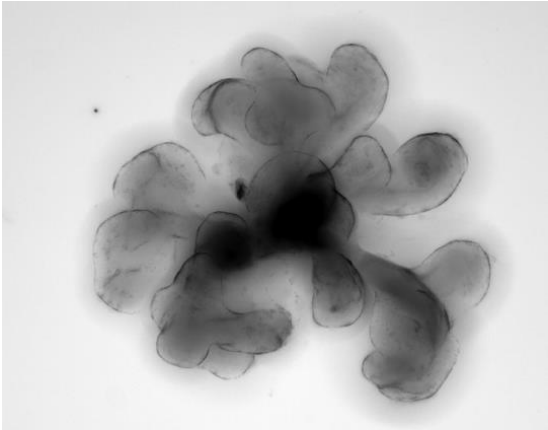

Supplementary Video 3: Mesenchyme-free lung bud culture
Time-lapse movie of a mesenchyme-free left lung bud dissected at E11.5 and cultured for 60h. (AVI 7.9 MB).

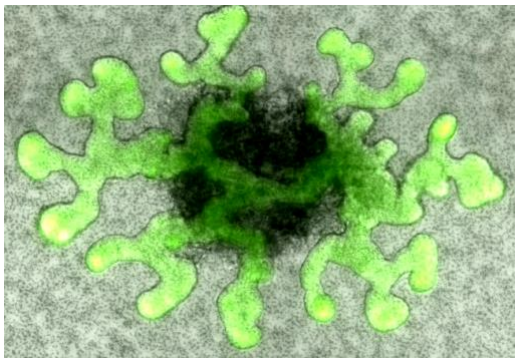

Supplementary Video 4: Mesenchyme-free ureteric bud culture
Time-lapse movie of a mesenchyme-free ureteric bud dissected at E11.5 and cultured for 60h. HoxB7/myr-Venus expression is shown in green, brightfield in grey. (AVI 10.8 MB).

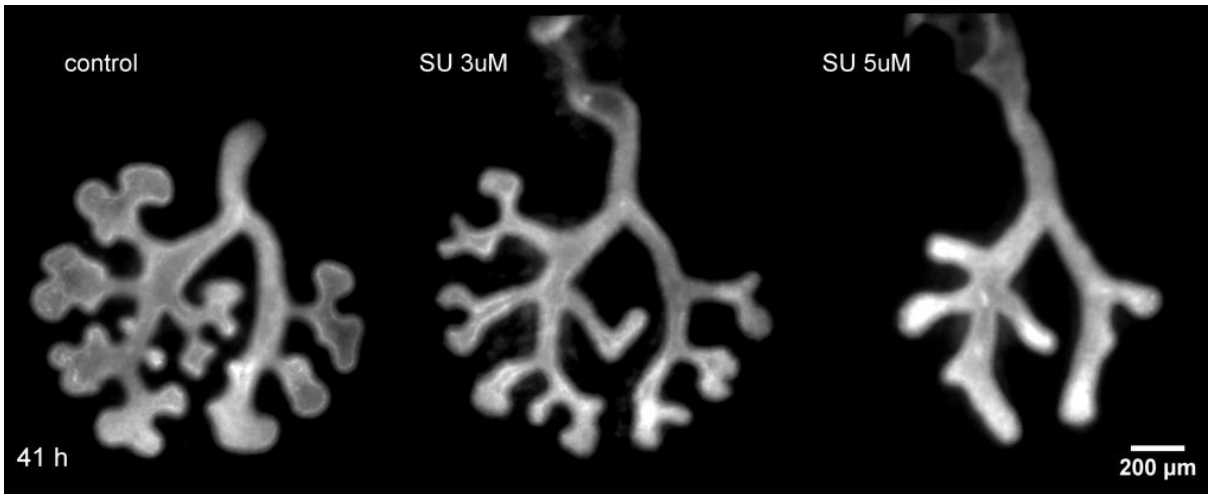

Supplementary Video 5: SU5402 time-lapse cultures of growing lungs
Culture of embryonic lungs (E11.5) under control conditions and with the treatment of the FGFR inhibitor SU5402 at different concentrations for 48h. (AVI 8.16 MB).

bioRxiv preprint doi: https://doi.org/10.1101/2020.06.22.166231; this version posted June 23, 2020. The copyright holder for this preprint (which was not certified by peer review) is the author/funder. All rights reserved. No reuse allowed without permission.

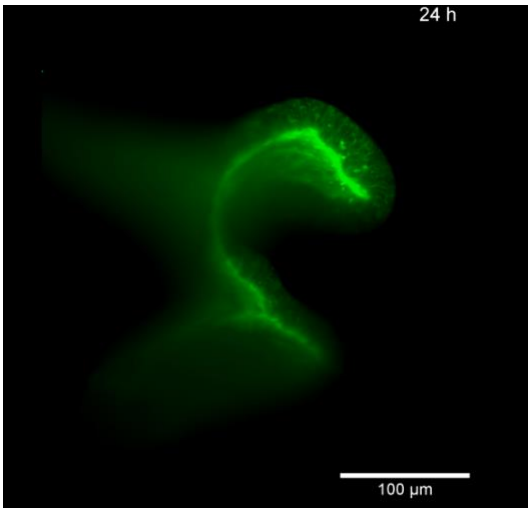

Supplementary Video 6: High-resolution light-sheet microscopy time-lapse imaging of lung bud elongation

Time-lapse movie showing the development of an E11.5 left lung rudiment carrying the Shh$^{GC/+}$; ROSA$^{mT/mG}$ construct. The specimen was mounted in a hollow cylinder made from low-melting-point agarose and filled with matrigel to replicate the native microenvironment and promote near-physiological growth. Imaging was done using the Zeiss Z.1 Lightsheet system for 34h. (AVI 2.38 MB).

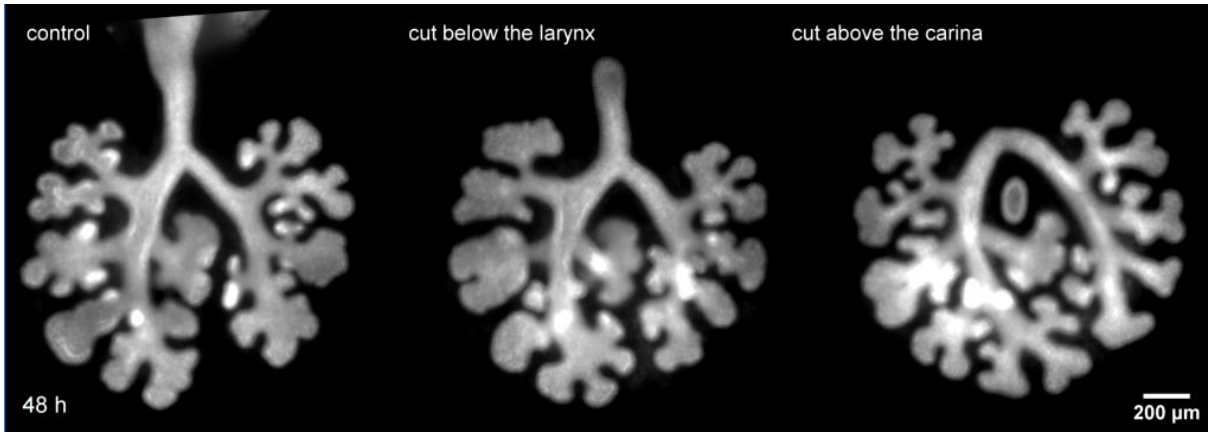

Supplementary Video 7: Time-lapse cultures of growing lungs with intact and cut trachea.

Culture of E11.5 embryonic lungs with intact trachea as control condition and with tracheas either cut below the larynx or above the carina for 48h. (AVI 11.8 MB).

bioRxiv preprint doi: https://doi.org/10.1101/2020.06.22.166231; this version posted June 23, 2020. The copyright holder for this preprint (which was not certified by peer review) is the author/funder. All rights reserved. No reuse allowed without permission.

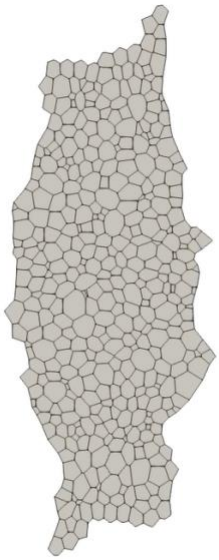

Supplementary Video 8: Tissue simulation with external force

Tissue growth simulation results of a vertex model when the initial configuration is subjected to a stretching force of 1.5 a.u. The parameters for the simulation are given in Supplementary Table 1.

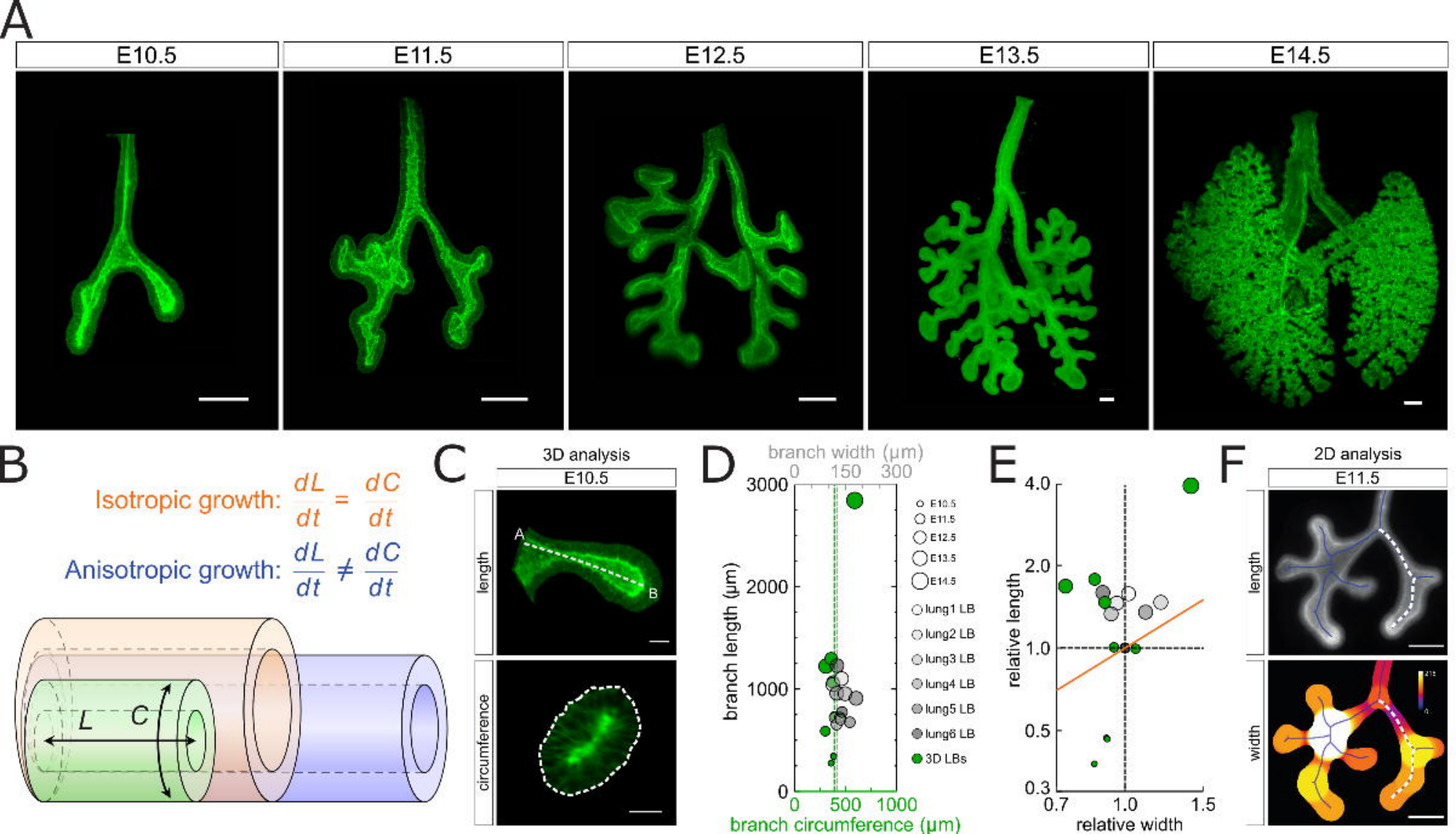
A
E10.5
E11.5
E12.5
E13.5
E14.5
B
Isotropic growth: $\frac{dL}{dt} = \frac{dC}{dt}$
Anisotropic growth: $\frac{dL}{dt} \neq \frac{dC}{dt}$
L
C
C
3D analysis
E10.5
length
circumference
A
B
D
branch width (µm)
0
150
300
3000
2000
1000
0
branch length (µm)
0
500
1000
branch circumference (µm)
E10.5
E11.5
E12.5
E13.5
E14.5
lung1 LB
lung2 LB
lung3 LB
lung4 LB
lung5 LB
lung6 LB
3D LBs
E
4.0
2.0
1.0
0.5
0.3
relative length
0.7
1.0
1.5
relative width
F
2D analysis
E11.5
length
width

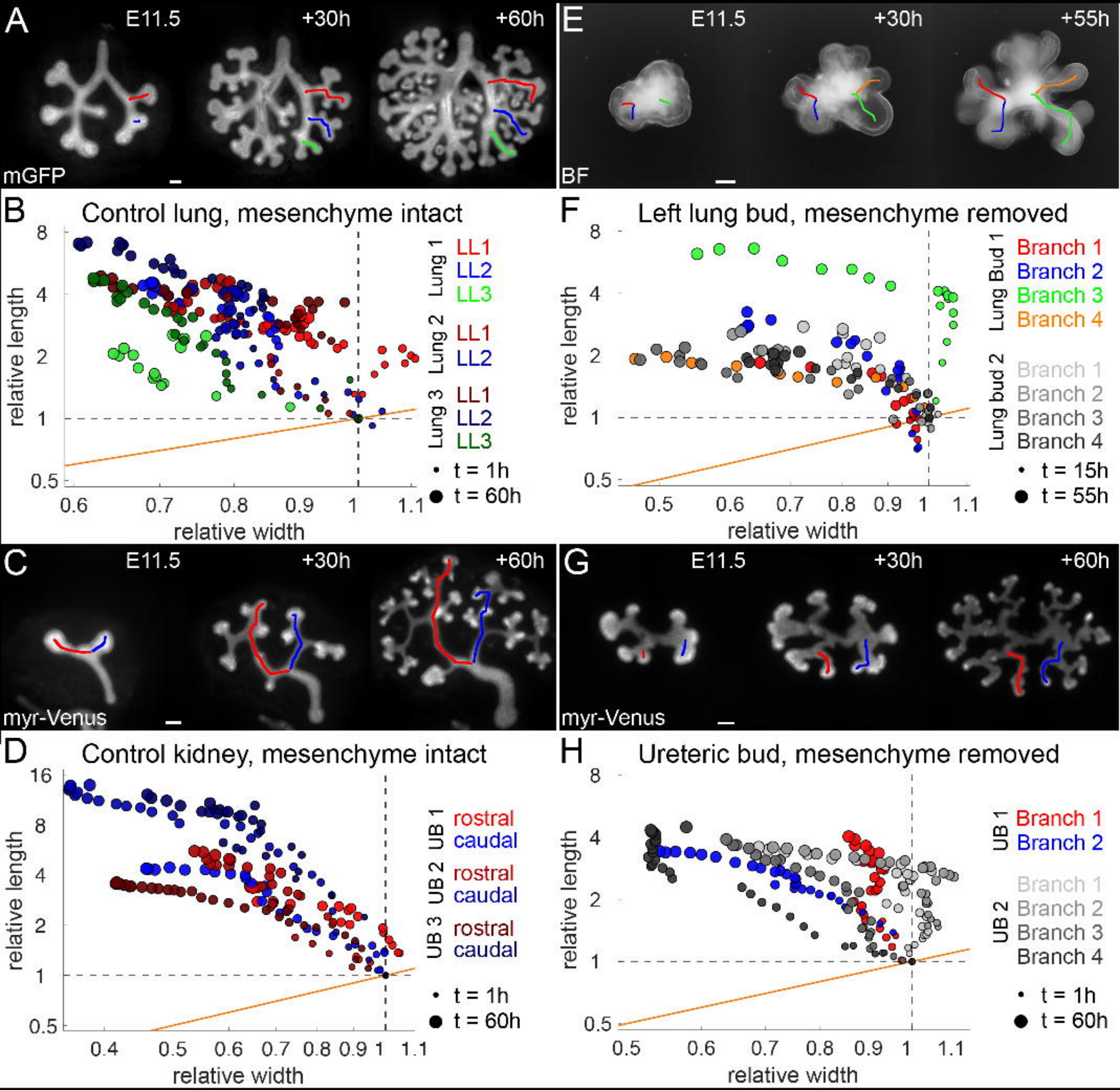
A
E11.5
+30h
+60h
mGFP
E
E11.5
+30h
+55h
BF
B
Control lung, mesenchyme intact
relative length
relative width
Lung 1
LL1
LL2
LL3
Lung 2
LL1
LL2
Lung 3
LL1
LL2
LL3
t = 1h
t = 60h
F
Left lung bud, mesenchyme removed
relative length
relative width
Lung Bud 1
Branch 1
Branch 2
Branch 3
Branch 4
Lung bud 2
Branch 1
Branch 2
Branch 3
Branch 4
t = 15h
t = 55h
C
E11.5
+30h
+60h
myr-Venus
G
E11.5
+30h
+60h
myr-Venus
D
Control kidney, mesenchyme intact
relative length
relative width
UB 1
rostral
caudal
UB 2
rostral
caudal
UB 3
rostral
caudal
t = 1h
t = 60h
H
Ureteric bud, mesenchyme removed
relative length
relative width
UB 1
Branch 1
Branch 2
UB 2
Branch 1
Branch 2
Branch 3
Branch 4
t = 1h
t = 60h

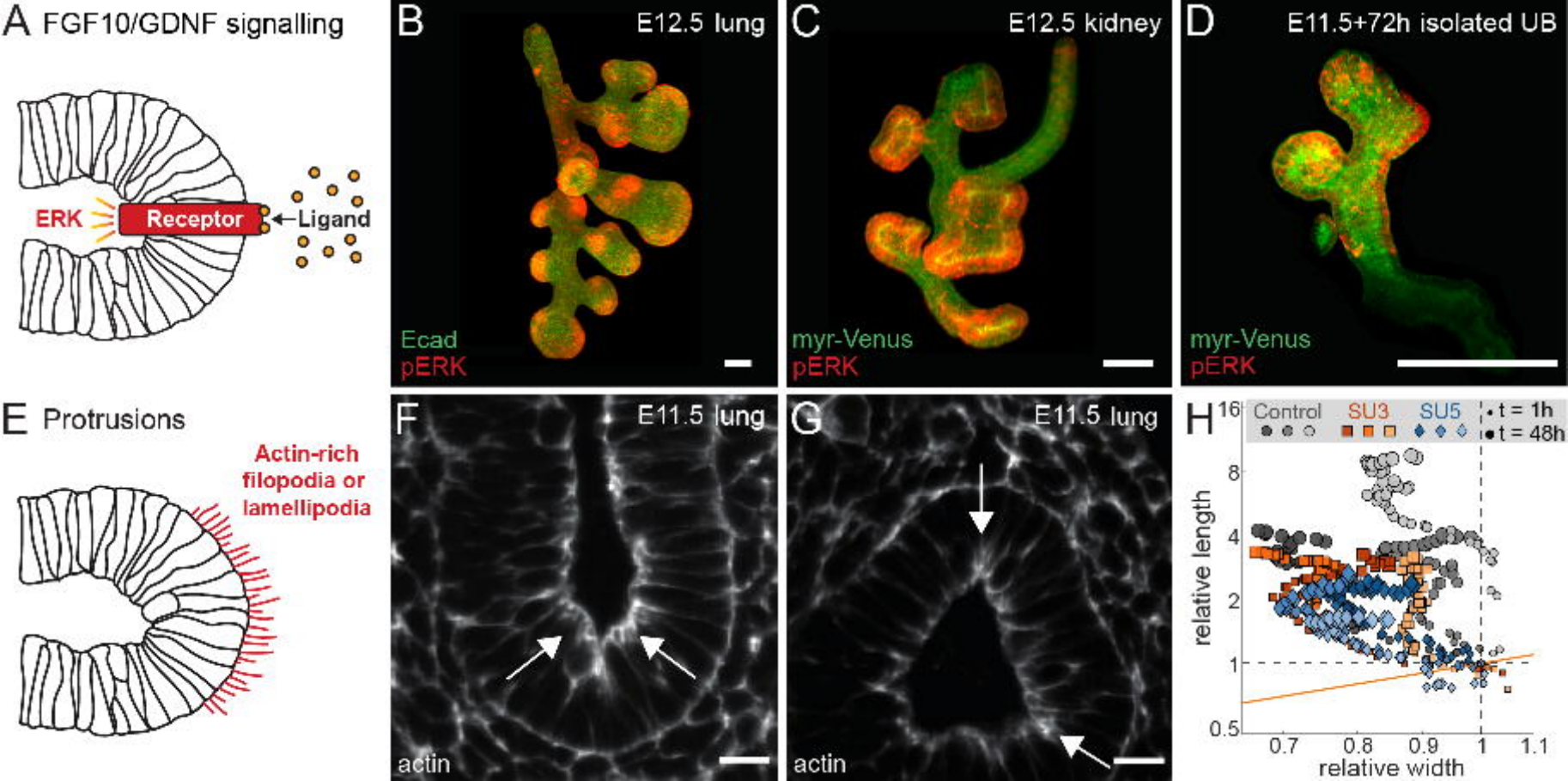
A FGF10/GDNF signalling
ERK
Receptor
Ligand
B
E12.5 lung
Ecad
pERK
C
E12.5 kidney
myr-Venus
pERK
D
E11.5+72h isolated UB
myr-Venus
pERK
E Protrusions
Actin-rich filopodia or lamellipodia
F
E11.5 lung
actin
G
E11.5 lung
actin
H
Control
SU3
SU5
t = 1h
t = 48h
relative length
relative width
16
8
4
2
1
0.5
0.7
0.8
0.9
1
1.1

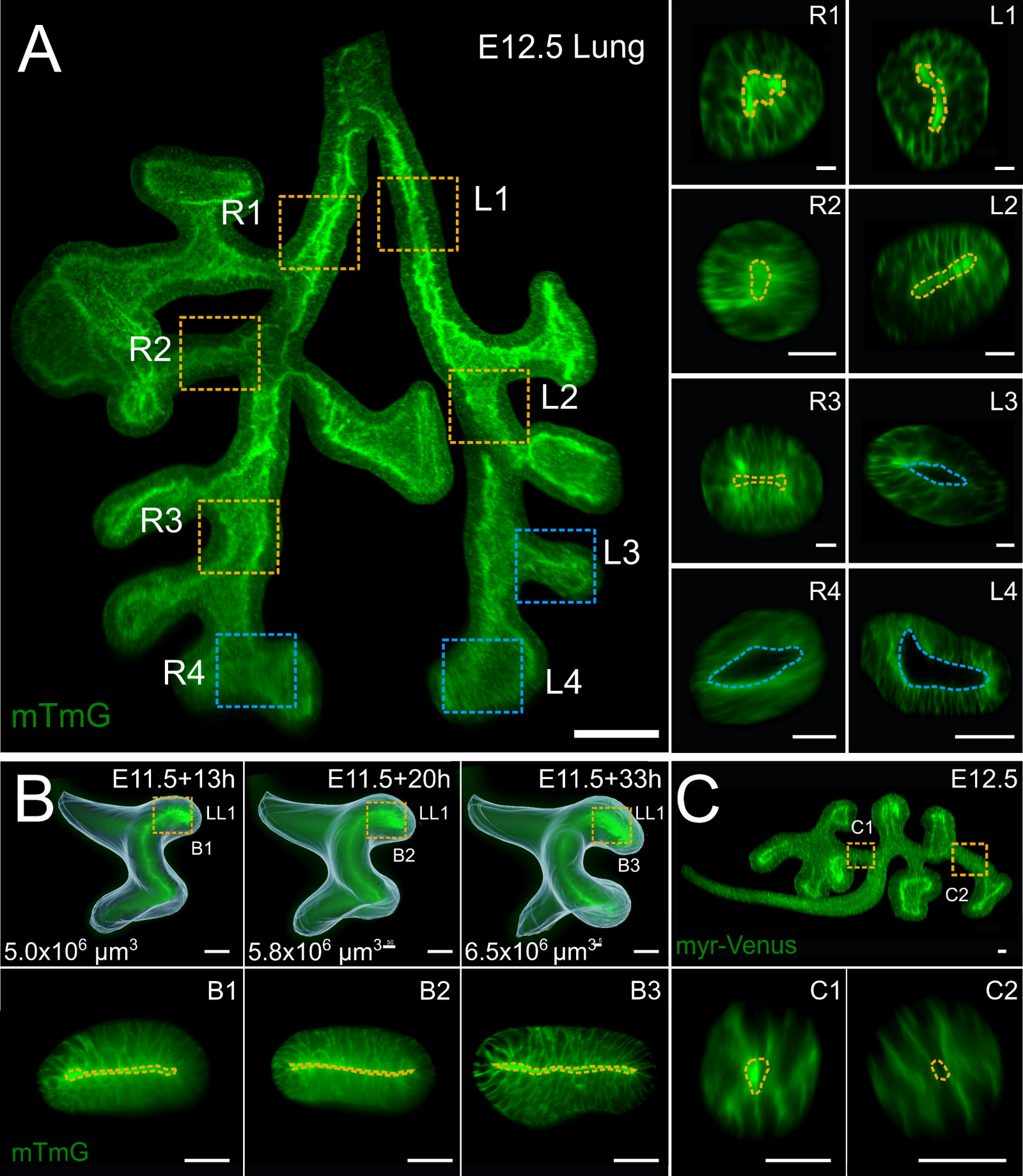
A
E12.5 Lung
R1
L1
R2
L2
R3
L3
R4
L4
mTmG
B
E11.5+13h
LL1
B1
5.0x10^6 μm^3
E11.5+20h
LL1
B2
5.8x10^6 μm^3
E11.5+33h
LL1
B3
6.5x10^6 μm^3
C
E12.5
C1
C2
myr-Venus
B1
B2
B3
C1
C2
mTmG

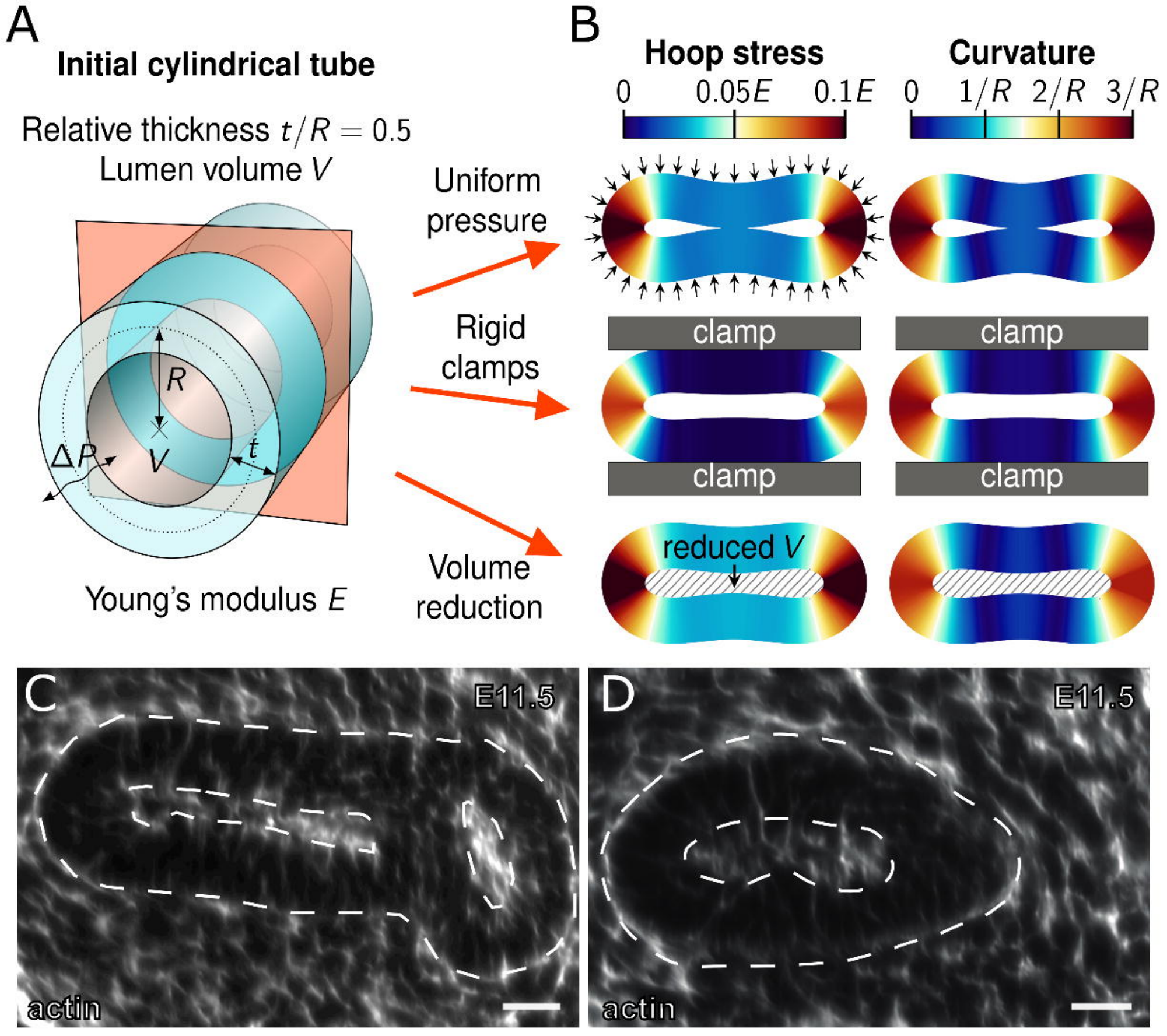
A
Initial cylindrical tube
Relative thickness $t/R = 0.5$
Lumen volume V
R
ΔP
V
t
Young's modulus E
Uniform pressure
Rigid clamps
Volume reduction
B
Hoop stress
0
0.05E
0.1E
Curvature
0
$1/R$
$2/R$
$3/R$
clamp
clamp
clamp
clamp
reduced V
C
E11.5
actin
D
E11.5
actin

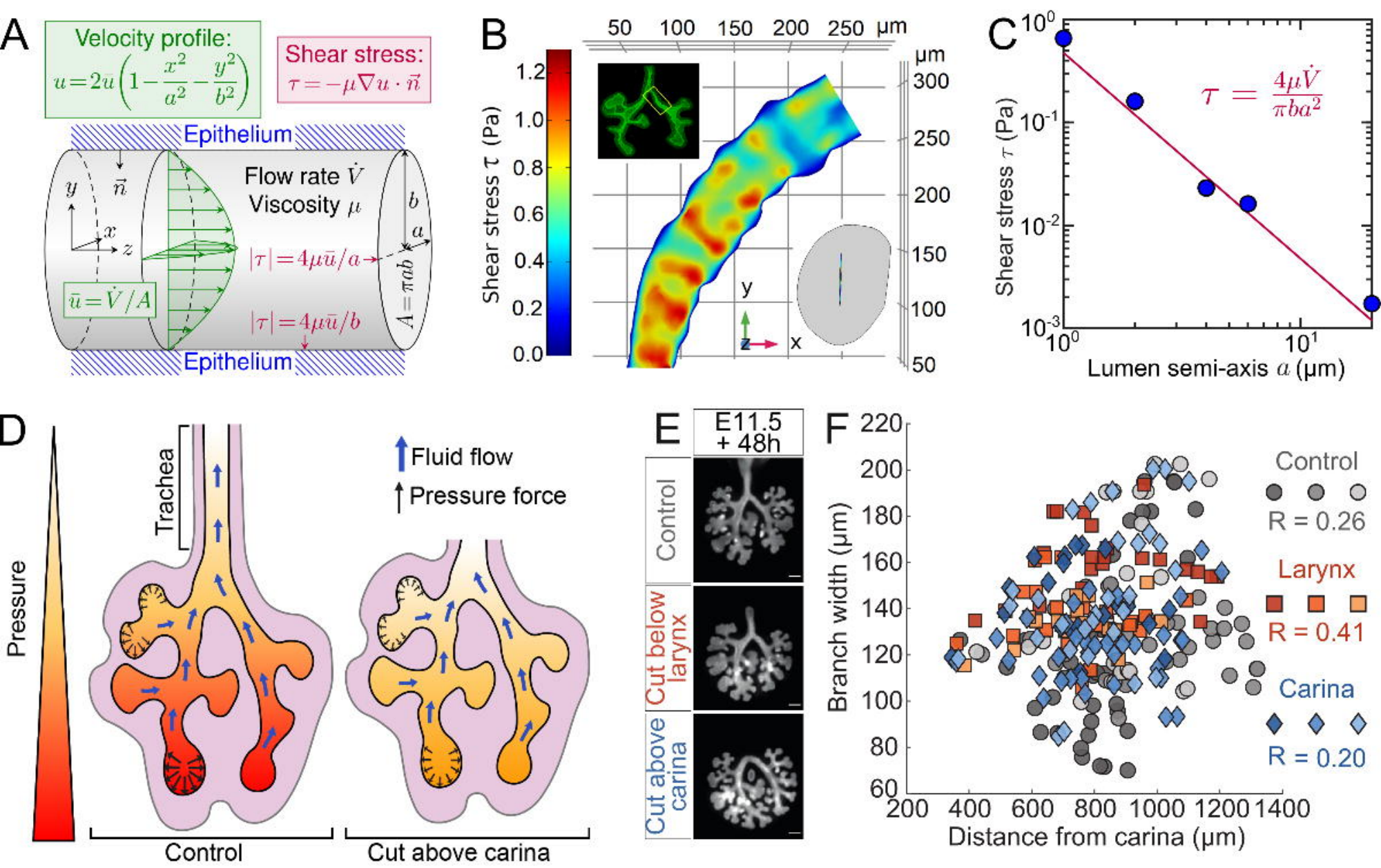
A
Velocity profile:
$u = 2\bar{u}\left(1 - \frac{x^2}{a^2} - \frac{y^2}{b^2}\right)$
Shear stress:
$\tau = -\mu \nabla u \cdot \vec{n}$
Epithelium
Flow rate $\dot{V}$
Viscosity μ
$|\tau| = 4\mu\bar{u}/a$
$|\tau| = 4\mu\bar{u}/b$
$\bar{u} = \dot{V}/A$
$A = \pi ab$
Epithelium
B
Shear stress τ (Pa)
μm
C
$\tau = \frac{4\mu\dot{V}}{\pi b a^2}$
Shear stress τ (Pa)
Lumen semi-axis a (μm)
D
Trachea
Fluid flow
Pressure force
Pressure
Control
Cut above carina
E
E11.5 + 48h
Control
Cut below larynx
Cut above carina
F
Branch width (μm)
Distance from carina (μm)
Control
R = 0.26
Larynx
R = 0.41
Carina
R = 0.20

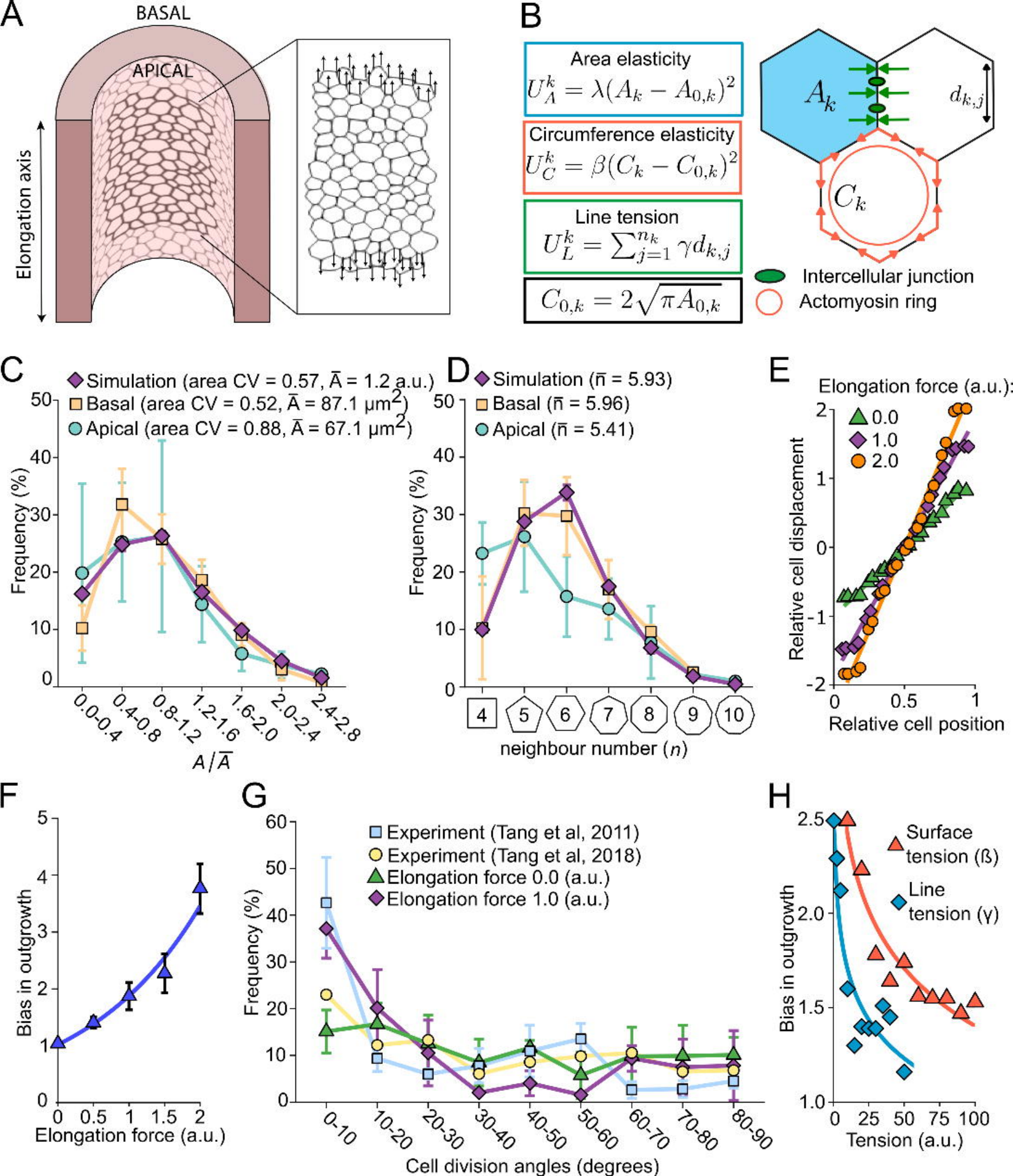
A
BASAL
APICAL
Elongation axis
B
Area elasticity
$U_A^k = \lambda(A_k - A_{0,k})^2$
Circumference elasticity
$U_C^k = \beta(C_k - C_{0,k})^2$
Line tension
$U_L^k = \sum_{j=1}^{n_k} \gamma d_{k,j}$
$C_{0,k} = 2\sqrt{\pi A_{0,k}}$
A_k
$d_{k,j}$
C_k
Intercellular junction
Actomyosin ring
C
Simulation (area CV = 0.57, Ā = 1.2 a.u.)
Basal (area CV = 0.52, Ā = 87.1 μm²)
Apical (area CV = 0.88, Ā = 67.1 μm²)
Frequency (%)
0.0-0.4
0.4-0.8
0.8-1.2
1.2-1.6
1.6-2.0
2.0-2.4
2.4-2.8
A/Ā
D
Simulation (n̄ = 5.93)
Basal (n̄ = 5.96)
Apical (n̄ = 5.41)
Frequency (%)
neighbour number (n)
E
Elongation force (a.u.):
0.0
1.0
2.0
Relative cell displacement
Relative cell position
F
Bias in outgrowth
Elongation force (a.u.)
G
Experiment (Tang et al, 2011)
Experiment (Tang et al, 2018)
Elongation force 0.0 (a.u.)
Elongation force 1.0 (a.u.)
Frequency (%)
0-10
10-20
20-30
30-40
40-50
50-60
60-70
70-80
80-90
Cell division angles (degrees)
H
Surface tension (ß)
Line tension (γ)
Bias in outgrowth
Tension (a.u.)